Radiative impact of improved global parameterisations of oceanic dry deposition of ozone and lightning-generated NO_x

Ashok K. Luhar[1], Ian E. Galbally[1], Matthew T. Woodhouse[1]

[1]CSIRO Oceans and Atmosphere, Aspendale, 3195, Australia

Correspondence to: Ashok K. Luhar (ashok.luhar@csiro.au)

Abstract. We investigate the radiative impact of recent process-based improvements to oceanic ozone dry deposition parameterisation and empirical improvements to lightning-generated NO_x (LNO_x) parameterisation by conducting a 5-year simulation of the Australian Community Climate and Earth System Simulator – United Kingdom Chemistry and Aerosol (ACCESS-UKCA) global chemistry-climate model, with radiative effects of ozone, methane and aerosol included. Compared to the base parameterisations, the global consequences of the two improved parameterisations on atmospheric composition are dominated by the LNO_x change~~s~~ (which increases the LNO_x production from 4.8 to 6.9 Tg N yr^{-1}) and include (a) an increase in the O_3 column of 3.75 DU ~~or 11.7%~~ and this O_3 change is centred on the tropical upper troposphere where ozone is most effective as a radiative forcer~~;~~, (b) a decrease of 0.64 years in the atmospheric lifetime of methane due to an increase in hydroxyl radical (OH), which corresponds to a decrease of 0.31 years in the methane lifetime per Tg N (nitrogen) change in LNO_x~~;~~ ~~and~~ (c) an increase of 6.7% in the column integrated condensation nuclei concentration; and (d) a slight increase in high-level cloud cover. The dry deposition improvement results in a relatively small increase of 4.4 mW m^{-2} in the global all-sky net downward top-of-atmosphere (TOA) radiative flux (which is akin to instantaneous radiative forcing). But this increases to 86 mW m^{-2} when the improved LNO_x parameterisation ~~(which increases the LNO_x production from 4.8 to 6.9 Tg N yr^{-1})~~ is also used. Other global radiative changes from the use of the combined two parameterisations include an increase in the downward longwave radiation and a decrease in the downward shortwave radiation at the Earth's surface. The indirect effect of LNO_x ~~via OH~~ on aerosol and cloud cover can at least partly explain the differences in the shortwave flux at the surface. We estimate that for a reported uncertainty range of 5 ± 3 Tg N yr^{-1} in global estimates of LNO_x, the uncertainty ~~range~~ in the net downward TOA radiation ~~due to reported uncertainty range in global estimates of LNO_x~~ is~~could be as much as~~ ± 119 mW m^{-2}~~.~~. The corresponding uncertainly in the atmospheric methane lifetime is ± 0.92 years. ~~It is demonstrated that although the total global LNO_x production may be the same, how LNO_x is distributed spatially makes a difference to radiative transfer.~~ Thus, ~~LNO_x has a significant influence on the atmospheric lifetime of CH_4, and~~ the value of LNO_x used within a model will influence the effective radiative forcing (ERF) ~~and global warming potential~~ of anthropogenic methane, and influence the results of climate scenario modelling. ~~The inter-model uncertainty in the ERF for methane will be contributed to by the model choices of LNO_x.~~

1 Introduction

Apart from water vapour, carbon dioxide (CO_2), methane (CH_4), ozone (O_3), nitrous oxide (N_2O), and fluorinated gases are the principal greenhouse gases in the atmosphere. Being radiatively active, these gases play an important role in the Earth's energy budget and hence climate system. Together with aerosol~~s~~, their concentrations govern the impedance to transfer and loss from the atmosphere of radiative energy. ~~A r~~Radiative forcing ~~broadly refers to~~ is a change in the top-of ~~the~~-atmosphere (TOA) energy budget as a result of an imposed anthropogenic or natural perturbation~~,~~ (for example, changes in aerosol or greenhouse gas concentrations, in downwelling solar radiation, or in land use). The climate system responds to this change by cooling or warming. In the Sixth Assessment Report (AR6) of the United Nations Intergovernmental Panel on Climate Change (IPCC), an effective radiative forcing (ERF) is termed as a change in net downward radiative flux at the TOA following a perturbation, including effects of any adjustments in both tropospheric and stratospheric temperatures, water vapour, clouds, and some surface properties, for example surface albedo from vegetation changes, but excluding any changes due to the global surface air temperature change (Forster et al., 2021). According to the IPCC AR6, the total abundance-based anthropogenic ERF due to increases in long-lived well-mixed greenhouse gases over the years 1750–2019 is 3.32 ± 0.29 W m^{-2}, of which 2.16 ± 0.26 W m^{-2} is due to CO_2, 0.54 ± 0.11 W m^{-2} to CH_4, 0.21 ± 0.03 W m^{-2} to N_2O and 0.41 ± 0.08 W m^{-2} to total halogens (Forster et al., 2021). Ozone is a short-lived climate forcer (SLCF), with a globally-averaged ~~(chemical~~ lifetime of about 22 days in the troposphere (Young et al., 2013), and its anthropogenic ERF for the same years~~period~~ is estimated to be 0.47 ± 0.23 W m^{-2}, almost all (95%) of which is due to tropospheric O_3 changes. Thus, tropospheric O_3 provides the third largest anthropogenic ERF, and overall O_3 represents about 16% of the net anthropogenic ERF of 2.72 ± 0.76 W m^{-2}, the latter includes an aerosol ERF of -1.1 ± 0.6 W m^{-2} (Forster et al., 2021).

Ozone interacts with down-welling and up-welling solar (or shortwave) and terrestrial (or longwave) radiation. Any changes in the atmospheric distribution of O_3 contribute to changes in its radiative impact. Compared to the long-lived and well-mixed greenhouse gases, O_3 exhibits a highly spatially inhomogeneous distribution in the troposphere because of its short chemical lifetime compared to transport timescales, and therefore, it has strong radiative effects on regional scales.

Ozone is not emitted directly into the atmosphere but is formed in both the stratosphere and troposphere by photochemical reactions involving natural and anthropogenic precursor species. Ozone is an oxidant as well as a precursor to the formation of hydroxyl (OH) and hydroperoxyl radicals which play a critical role in the tropospheric chemical cycles of many trace gases, e.g., CH_4 and carbon monoxide (CO), and the production of aerosol. The tropospheric budget of O_3 is governed by its production through the photochemical oxidation of CH_4, CO and non-methane volatile organic compounds (NMVOC) in the presence of oxides of nitrogen (NO_x); removal by several chemical reactions; removal by dry deposition at surface of the Earth; and the downward transport of O_3 from the stratosphere.

This paper extends recent work on improvements to the oceanic O_3 dry deposition parameterisation (Luhar et al., 2018) and lightning-generated NO_x (referred to as LNO_x) parameterisation (Luhar et al., 2021) to investigate the impact on radiative

transfer of these improvements via the use of the global Australian Community Climate and Earth System Simulator – United Kingdom Chemistry and Aerosol (ACCESS-UKCA) chemistry-climate model. One of the primary purposes of improving these physico-chemical processes is to improve the overall performance of chemistry-climate and earth system models.

Dry deposition is a significant sink of O_3 (Galbally and Roy, 1980; Luhar et al., 2017; Clifton et al., 2020), affecting O_3 mixing ratio, and its long-range transport and lifetime. The improved dry deposition parameterisation by Luhar et al. (2018) is a mechanistic air–sea exchange scheme that accounts for the concurrent waterside processes of molecular diffusion, O_3 solubility, first-order chemical reaction of O_3 with dissolved iodide, and turbulent transfer. It is a significant improvement over the assumption in most chemical transport models that the controlling term of surface resistance in the scheme for dry deposition velocity of O_3 at the ocean surface is constant based on Wesely (1989) (see section 2.2), and results in~~leads to~~ a smaller averaged O_3 dry deposition velocity to the ocean (by a factor of 2–3), in better agreement with observations, and an increase in ~~and a larger~~ the tropospheric O_3 burden by 1.5% and a decrease in the methane lifetime by 0.8%.

Although LNO_x accounts for only about 10% of the global NO_x source, it has a disproportionately large contribution to the tropospheric burdens of O_3 and ~~the hydroxyl (~~OH~~) radical~~ (Dahlmann et al., 2011; Murray, 2016). It's ~~The~~ impact on ~~both~~ O_3 concentration, ~~and~~ the CH_4 lifetime (against loss by tropospheric OH) and aerosol in turn influences atmospheric radiative transfer. Schumann and Huntrieser (2007) report a large uncertainty range of 5 ± 3~~2–8~~ Tg nitrogen (N) yr^{-1} in the global amount of LNO_x generated. Other estimates of global LNO_x emissions include 6 ± 2 Tg N yr^{-1} (Martin et al., 2007) and ~ 9 Tg N yr^{-1} (Nault et al., 2017).

[As a side note, while we estimate the globally-averaged direct energy dissipated from lightning flashes to be only ~ 0.2 mW m^{-2}~~,~~ (see the Supplement S1 for details), the radiative energy retained in the atmosphere due to the net impact of LNO_x on O_3 production and CH_4 loss is ~ 40 mW m^{-2} per Tg N yr^{-1} produced due to lightning (see section 3.5~~3~~), which implies a radiative impact of ~ 80 – 320 mW m^{-2} corresponding to the above LNO_x range of 5 ± 3 Tg N yr^{-1}~~,~~. The atmospheric radiative change resulting from lightning ~~which~~ is thus roughly three orders of magnitude larger than the direct energy release associated with the lightning flashes, a remarkable atmospheric amplifier.]

In most global chemistry models, lightning flash rates used to estimate LNO_x are expressed in terms of convective cloud-top height via Price and Rind's (1992) (PR92) empirical parameterisations for land and ocean. Luhar et al. (2021) tested the PR92 flash-rate parameterisations within ACCESS-UKCA using satellite lightning data and found that while the PR92 parameterisation for land performs well, the oceanic parameterisation underestimates the observed global mean flash frequency by a factor of approximately 30, leading to LNO_x being underestimated proportionally over the ocean. Luhar et al. (2021) improved upon the PR92 flash-rate parameterisations (see section 2.3). They showed that the improved parameterisation for land performs very similar to the corresponding PR92 one in simulating the continental spatial distribution of the global lightning flash rate. The improved oceanic parameterisation simulates the oceanic and total flash-rate observations much more accurately. Luhar et al. (2021) used the improved flash-rate parameterisations in ACCESS-UKCA and found that they resulted

in a considerable impact on the modelled tropospheric composition compared to the default PR92 parameterisations, including an increase in the global LNO_x increased from 4.8 to 6.6 Tg N yr^{-1}; an increase in the ozone O_3 burden by 8.5%; a 13% increase in the volume-weighted global OH; and a decrease in the methane lifetime by 6.7%. The improved flash-rate parameterisations also led to improved simulation of tropospheric NO_x and ozone in the Southern Hemisphere and over the ocean compared to observations. Luhar et al. (2021) did not examine any changes in aerosol due to the changes in LNO_x (this is done in the present work).

~~The improved LNO_x parameterisation by Luhar et al. (2021) is a refinement over the widely used lightning flash rate parameterisation developed by Price and Rind (1992) (PR92), especially for the ocean for which the PR92 parameterisation greatly underestimates the lightning flash rate and therefore results in a lower tropospheric O_3 burden.~~

We conduct a number of ACCESS-UKCA model simulations to quantify the effects of the above two parameterisation changes on the net downward shortwave (SW) and longwave (LW) radiative fluxes at ~~the top of the atmosphere (~~TOA~~)~~, and the downward surface SW and LW radiative fluxes, and these are reported here. Part of these changes arises due to the changes in atmospheric lifetime of CH_4, and that is included in the discussion. The calculated changes in the radiative fluxes are also put in the context of the IPCC anthropogenic ERF estimates.

2 The ACCESS-UKCA global chemistry-climate model and model setup

We use the United Kingdom Chemistry and Aerosol (UKCA) global atmospheric composition model (Abraham et al., 2012; https://www.ukca.ac.uk) coupled to ACCESS (Australian Community Climate and Earth System Simulator) (Bi et al., 2013; Woodhouse et al., 2015). In the simulations carried out here, ACCESS is essentially the same as the U.K. Met Office's Unified Model (UM) (vn8.4) as the ACCESS specific land-surface and ocean components are not invoked. The UM's original land-surface scheme (viz. JULES) is used and the model is run in atmosphere-only mode with prescribed monthly-mean sea surface temperature (SST) and sea ice fields. The atmosphere component of the UM vn8.4 is the Global Atmosphere (GA 4.0) (Walters et al., 2014). The UKCA configuration used here is the so-called StratTrop (or Chemistry of the Stratosphere and Troposphere (CheST)) (Archibald et al., 2020), which also includes the GLObal Model of Aerosol Processes (GLOMAP)-mode aerosol scheme (Mann et al., 2010). Dust is treated outside of GLOMAP-mode as per the scheme described by Woodward (2001).

The tropospheric chemistry scheme includes the chemical cycles of O_x, HO_x and NO_x, and the oxidation of CO, CH_4, and other volatile organic carbon (VOC) species (for example, ethane, propane, and isoprene). The Fast-JX photolysis scheme reported by Neu et al. (2007) and Telford et al. (2013) is used. Ozone~~O_3~~ is coupled interactively between chemistry and radiation. The aerosol section includes sulphur chemistry. The total number of chemical reactions, including those in aerosol chemistry, is 306 across 86 species.

The horizontal resolution of the atmospheric model is 1.875° longitude × 1.25° latitude, with 85 staggered terrain-following hybrid-height levels extending from the surface to 85 km in altitude (the so-called N96L85 configuration). The vertical

resolution becomes coarser with height, with the lowest 65 levels (altitudes up to ~ 30 km) located within the troposphere and lower stratosphere. The model's dynamical timestep is 20 min, and the UKCA chemical solver is called every 60 min.

A global monthly-varying emissions database for reactive gases and aerosol~~s~~ is used, which includes both anthropogenic, biomass burning and natural components (Woodhouse et al., 2015; Desservettaz et al., 2022). Pre-2000 anthropogenic emissions are prescribed from the Atmospheric Chemistry and Climate Model Intercomparison Project (ACCMIP) (Lamarque et al., 2010), and post-2000 from Representative Concentrations Pathway (RCP) 6.0 scenario (van Vuuren et al. 2011). Biomass burning emissions are from the GFED4s database (van der Werf et al., 2017). Concentrations of CO_2, CH_4, N_2O and O_3 depleting substances are prescribed instead of emissions and are from the Coupled Model Intercomparison Project Phase 5 (CMIP5) and RCP6.0 recommendations. Terrestrial b~~B~~iogenic emissions are from the Model of Emissions of Gases and Aerosols from Nature – Monitoring Atmospheric Composition and Climate dataset~~project~~ (MEGAN-MACC; Sindelarova et al., 2014), excepting soil NO_x which is taken from the "global emissions initiative" (GEIA) project (https://www.geiacenter.org; last access 11 August 2014). The "present and future surface emissions of atmospheric compounds" (POET) database (Olivier et al., 2003) is used for oceanic ethane, propane, and CO emissions. Details of required emissions of other species, and their original sources, including biogenic emissions, chemical precursors and primary aerosol are given by Woodhouse et al. (2015).

2.1 ~~Model's r~~Radiation scheme ~~for gases~~

UKCA is coupled to ACCESS's ~~uses the broadband~~ radiation scheme ~~of Edwards and Slingo (1996), updated and described by Walters et al. (2014),~~ to determine the impact of the UKCA aerosol and radiatively active trace gases (normally O_3, CH_4, N_2O and O_3 depleting substances) for any specific model configuration. ~~radiatively active trace gases and aerosols, including clouds, on radiative fluxes, from which heating rates and related quantities may be determined. As UKCA is coupled to this radiation scheme, it is possible calculate the radiative influence of the UKCA gaseous tracer fields (normally O_3, CH_4, N_2O and O_3 depleting substances) for any specific model configuration. In the present UKCA configuration, mixing ratios of O_3, CH_4, N_2O are coupled to the radiation code where O_3 is passed from the modelled 3-D fields.~~For radiatively active trace gases, t~~T~~he Edwards and Slingo (1996) scheme, with updates described by Walters et al. (2014), is used. ~~uses the so-called correlated-k method for gaseous absorption for major gases with 6 bands in the shortwave and 9 bands in the longwave regions of the spectrum. In each spectral band, total transmission is determined by summing the results of a number of quasi-monochromatic calculations, each carried out using a two-stream approximation, in which the angular variation of the radiance field is represented simply by an upward and a downward diffuse flux, together with a direct solar flux in the shortwave region. Twenty one k-terms are used f~~For the major gases (i.e., the dominant absorbers) in the shortwave bands, ~~,~~ a~~A~~bsorption by water vapour (H_2O), O_3, CO_2 and oxygen (O_2) is included. The treatment of O_3 absorption is as described by Zhong et al. (2008). ~~Forty-seven k-terms are used f~~For the major gases in the longwave bands, ~~,~~ a~~A~~bsorption by H_2O, O_3, CO_2, CH_4, N_2O, and halocarbons is included. The treatment of CO_2 and O_3 absorption is as described by Zhong and Haigh (2000). Of the major

gases considered, H_2O and O_3 are prognostic, whilst other gases are prescribed using either fixed or time-varying mass mixing ratios and assumed to be well mixed. The method of equivalent extinction (Edwards, 1996) is used for the minor gases (i.e., the weak absorbers) in each band.

In the present UKCA configuration, aerosol (direct scattering and absorption), O_3, CH_4, N_2O are coupled to the radiation code where aerosol and O_3 are passed from the modelled 3-D fields. Aerosol additionally influences the large-scale cloud and precipitation schemes through the cloud droplet number concentration, whereas convective rainfall and cloud formation are not directly coupled to the model aerosol scheme but can be indirectly influenced via changes in radiation which can in turn influence properties such as temperature and moisture (Abraham et al., 2012; Bellouin et al., 2013; Fiddes et al., 2018).

LNO_x is also a precursor of nitrate aerosol in the upper troposphere, and this aerosol can influence atmospheric radiation (Tost, 2017). However, ACCESS-UKCA as used here does not include nitrate aerosol, which is also the case with most global chemistry-climate models. ~~There may be a small negative contribution to the net downward TOA radiative flux through formation of nitrate aerosols as LNO_x is increased, but most global chemistry-climate models (including ACCESS-UKCA) do not include nitrate aerosols (e.g., only three of the AerChemMIP models have this capability).~~ Of the ten CMIP6 Earth system models that conducted the AerChemMIP (Aerosol and Chemistry Model Intercomparison Project) simulations, only three included nitrate aerosols (Thornhill et al., 2021b). Naik et al. (2021) report that there is a relatively small negative contribution to ERF through formation of nitrate aerosols. Recently, a nitrate scheme has been incorporated in UKCA (Jones et al., 2021) and this should be tested in the future to examine the impact of nitrate aerosol from lightning on radiation. Although the model does not include a nitrate aerosol scheme, the LNO_x changes would impact aerosol through perturbations to background tropospheric oxidants, for example increases in aerosol abundances due to faster oxidation rates of sulfur to sulfate as LNO_x is increased (Murray, 2016).

2.2 Ozone dry deposition scheme for the ocean

Dry deposition flux of O_3 to Earth's surface is ~~usually~~ modelled as the product of O_3 concentration in the air near the surface and a (downward) dry deposition velocity, v_d, which is calculated as (Wesely, 1989)

$$v_d = \frac{1}{r_a + r_b + r_c}, \quad (1)$$

where r_a is the aerodynamic resistance which is the resistance to transfer by turbulence in the atmospheric surface layer, r_b is the atmospheric viscous (or quasi laminar) sublayer resistance which is the resistance to movement across a thin layer (0.1 – 1 mm) of air that is in direct contact with the surface, and r_c is the surface resistance which is the resistance to uptake by the surface itself. Various parameterisations are used to calculate these resistances. r_c is the dominant term in Eq. (1) for O_3 dry deposition to water surfaces, and it is routinely assumed that r_c for water is constant at ≈ 2000 s m^{-1} following Wesely's (1989) widely used dry deposition parameterisation. Most global chemical transport models, e.g. CAM-chem (Lamarque et

al., 2012), GEOS-Chem (Mao et al., 2013) and UKCA, have followed this approach thus far by default, with ACCESS-UKCA using $r_c = 2200$ s m^{-1}.

Recently, Luhar et al. (2017, 2018) concluded that the use of the above constant r_c approach in ACCESS-UKCA overestimates O_3 deposition velocities to the ocean by as much as a factor of 2 to 4 compared to measurements, and does not simulate their observed spatial variability well. Luhar et al. (2018) developed a two-layer process-based parameterisation for r_c that accounts for the concurrent waterside processes of molecular diffusion, O_3 solubility, first-order chemical reaction of O_3 with dissolved iodide, and turbulent transfer, and found that this parameterisation described the O_3 deposition velocities much better and reduced the global oceanic O_3 deposition to approximately one-third of the default value obtained using Wesely's (1989) r_c approach. Using the new/improved parameterisation, Luhar et al. (2018) estimated an oceanic dry deposition of 98.4 ± 30.0 Tg O_3 yr^{-1} and a global one of 722.8 ± 87.3 Tg O_3 yr^{-1} (averaged over years 2003–2012), which can be compared with the respective values 340 Tg O_3 yr^{-1} and 978 ± 127 Tg O_3 yr^{-1} obtained by Hardacre et al. (2015) based on 15 global chemistry transport models (for year 2001) using Wesely's scheme, demonstrating the large reduction in the oceanic value using the new parameterisation. The new approach has recently been evaluated by other researchers in both global and regional models with various changes to input parameter values (Loades et al., 2020; Pound et al., 2020; Barten et al., 2021).

We use both the default and new oceanic dry deposition parameterisations (the latter corresponding to the Ranking 1 configuration in Table 1 of Luhar et al. (2018)).

2.3 Lightning-generated NO_x

NO_x, which is a mixture of nitrogen dioxide (NO_2) and nitric oxide (NO), acts as a precursor to O_3 and OH, which are the principal tropospheric oxidants. ~~The upper troposphere is where O_3 is most potent as a greenhouse gas.~~ Lightning mainly happens in the tropics related to deep atmospheric convection and is the primary source of NO_x in the middle to upper troposphere where lightning is mostly discharged. A tropospheric ozone radiative kernel for all-sky conditions (i.e., clear, cloud overcast, and partially cloudy skies) derived by Rap et al. (2015) suggests that ozone changes in the tropical upper troposphere are up to 10 times more efficient in altering the Earth's radiative flux than other regions.

As stated earlier, Schumann and Huntrieser (2007) report a range of 5 ± 3~~2 – 8~~ Tg nitrogen (N) yr^{-1} produced by lightning globally. The range of global LNO_x in 16 ACCMIP models in CMIP5 varied between 1.2 to 9.7 Tg N yr^{-1} (Lamarque et al., 2013), whereas in five earth system models in the Coupled Model Intercomparison Project Phase 6 (CMIP6) LNO_x ranged between 3.2 to 7.6 Tg N yr^{-1} (Griffiths et al., 2021; Naik et al., 2021) for the present-day (nominal year 2000) conditions.

The LNO_x amount in most global models is calculated as

$$LNO_x = P_{NO} \times F, \quad (2)$$

where P_{NO} is the quantity of NO generated per lightning flash, and F is the flash rate. F is calculated at every model time step within a model grid, and partitioned into cloud-to-ground (CG) and intracloud (IC) flash components. An emission factor of the amount of NO generated per CG/IC flash is applied, and the calculated mass of NO is then distributed vertically in the grid column (Luhar et al., 2021).

Of all the past techniques used to determine lightning flash rate in global chemistry-climate models and chemical transport models, including ACCESS-UKCA, the PR92 parameterisations are the most commonly used ones. They (or very similar) have also been used in most CMIP5 and CMIP6 models.

The PR92 parameterisations for lightning flash rate (flashes per minute) over land (F_L) and ocean (F_O) are

$$F_L = 3.44 \times 10^{-5} H^{4.9}, \quad (3)$$

$$F_O = 6.4 \times 10^{-4} H^{1.73}, \quad (4)$$

where H is the height of the convective cloud top (km), which is passed from the model's convection parameterisation scheme~~ve component~~. The above parameterisations yield flash rates over the ocean that are smaller by approximately 2 to 3 orders of magnitude compared to those calculated for clouds over land.

The oceanic parameterisation Eq. (4) is known to greatly underestimate flash rates. Recently, Luhar et al. (2021) evaluated the PR92 parameterisations for the year 2006 and found that ~~-~~while the land parameterisation Eq. (3) gave satisfactory predictions~~,~~ (an average value of 32.5 flashes s^{-1} compared to 34.9 flashes s^{-1} obtained from satellite observations), the oceanic parameterisation Eq. (4) yielded a global mean value of 0.33 flashes s^{-1} over the ocean, a much smaller value than the observed 9.16 flashes s^{-1} ~~obtained from satellite observations~~. They formulated the following improved flash-rate parameterisations using the scaling relationships between thunderstorm electrical generator power and storm geometry developed by Boccippio's (2002), together with available data:

$$F_L = 2.40 \times 10^{-5} H^{5.09}, \quad (5)$$

$$F_O = 2.0 \times 10^{-5} H^{4.38}. \quad (6)$$

Flash rates obtained using Eq. (6) are approximately two orders of magnitude greater than those obtained using Eq. (4). Eq. (5) performed very similar to Eq. (3), giving an average value of 35.9 flashes s^{-1} compared to 34.9 flashes s^{-1} obtained from satellite observations, and the new/improved marine parameterisation Eq. (6) gave a global mean marine flash rate of 8.84 flashes s^{-1}, which is very close to the observed value of 9.16 flashes s^{-1}.

With $P_{NO} = 330$ moles NO per flash, the use of Eqs. (5) and (6) in ACCESS-UKCA increased the mean total global LNO_x by 38% from the base value of 4.8 Tg N yr^{-1} (Luhar et al. (2021), with a considerable impact on the tropospheric composition ~~with a corresponding increase in tropospheric O_3 burden~~as stated in Section 1.

We investigate the radiative effects of this change ~~in O_3 due to the change~~ in LNO_x.

2.4 Global model simulations

We conducted the following six ACCESS-UKCA simulations for the years 2004–2010 ~~with O_3 and CH_4 radiation feedbacks included (except Run E)~~. Considering the first two simulation years as model spin-up time, the output from the model for the five-year period 2006–2010 was used for the analysis reported below:

- Base run (Run A): Default model run, with $r_c = 2200$ s m^{-1} in the oceanic O_3 deposition, and the PR92 lightning flash-rate parameterisation~~s~~ (LNO_x = 4.8 Tg N yr^{-1}),
- Run B: New process-based oceanic O_3 deposition scheme and the PR92 lightning flash-rate parameterisation~~s~~ (LNO_x = 4.8 Tg N yr^{-1}),
- Run C: New process-based oceanic O_3 deposition scheme and new lightning flash-rate parameterisation~~s~~ (LNO_x = 6.9 Tg N yr^{-1}),
- Run D: New process-based oceanic O_3 deposition scheme, and the PR92 lightning flash-rate parameterisation~~s~~ but scaled uniformly by a factor of 1.44 to give the total global LNO_x the same as Run C (LNO_x = 6.9 Tg N yr^{-1}) (to check the impact of the difference in spatial distribution of the lightning flashes),
- Run E: Same as Run C, but without the CH_4 radiation feedback (to quantify its ~~separate out the~~ individual radiative impact~~effects of O_3 alone~~) (LNO_x = 6.9 Tg N yr^{-1}), and
- Run F: New process-based oceanic O_3 deposition scheme and LNO_x = 0.

Apart from the above changes, the rest of the model setup is the same as described in Section 2 of Luhar et al. (2021). The simulations were nudged to the ECMWF's ERA-Interim reanalyses in the free troposphere involving horizontal wind components and potential temperature given on pressure levels at 6-hourly intervals (Dee et al., 2011; https://www.ecmwf.int/en/forecasts/datasets/reanalysis-datasets/era-interim). Each model run was initialised using a previously spun-up model output with nudging and the default lightning and dry deposition schemes. The use of nudging does not allow the model changes to adjust synoptic-scale meteorology; hence the results here represent instantaneous radiative responses in the climate system, unlike the ERF which is the sum of the instantaneous radiative forcing (IRF) and the contribution from such adjustments. Due to nudging, responses in the simulation may be dampened, but can be attributed directly to the model perturbations (Fiddes et al., 2018).

The model results were averaged over 5-years for the globe, tropics, extra-tropics, land, and sea~~, Northern Hemisphere and Southern Hemisphere~~. Differences between the base model run and the other runs were calculated and~~were~~ indexed as follows on the x-axis in relevant plots presented below.

- 1 (dep.) = Run B – Base
- 2 (dep. + LNO_x) = Run C – Base
- 3 (dep. + scaled LNO_x) = Run D – Base

- 4 (dep. + LNO_x + no CH_4) = Run E – Base
- 5 (dep. + no LNO_x) = Run F – Base

3 Results and discussion

Monthly-averaged model output for various radiative components and chemical species is used in the following.

3.1 Modelled ozone, methane lifetime and aerosol

Table 1 summarises the global-averaged impact of the various parameterisation changes. With the new dry deposition scheme (Run B), the tropospheric O_3 burden increases by 1.5% over the base run. With both the new dry deposition and LNO_x schemes (Run C) this increase in the tropospheric O_3 burden is by 11.7%. Similarly, the increase in the total O_3 column is by 0.14 DU for the new dry deposition scheme and 3.75 DU for the new dry deposition and LNO_x schemes combined. The global distribution of the O_3 column difference between Run C and the base run in Figure 1a shows that the biggest differences as high as ≈ 8 DU occur in the tropics between 140°W –100°E.

Changes in LNO_x and O_3 also affect the global mean lifetime of CH_4 due to loss by OH (τ_{CH_4}) in the troposphere (Labrador et al., 2004). As Table 1 shows, there is a relatively small decrease of 0.06 years in τ_{CH_4} when the new oceanic O_3 dry deposition scheme is used and this decrease is 0.64 years when the improved LNO_x parameterisation is also used. In Table 1, the modelled methane lifetimes are lower than the ACCMIP multi-model mean 9.7 ± 1.5 years reported by Naik et al. (2013), which, as pointed out by Luhar et al. (2021), could be due to a higher tropospheric burden of non-lightening related NO_x in ACCESS-UKCA and/or a more intense photolysis. However, because we are mainly focusing on differences with respect to the base run, the lower absolute values of τ_{CH_4} from ACCESS-UKCA are not considered to be as pertinent.

Table 1 also presents the modelled global-averaged column integrated condensation nuclei (CN, > 3 nm dry diameter, also denoted as N_3) or aerosol number concentration. The column CN concentration increases with LNO_x and this increase for Run C is 6.7% over the base run. The global distribution of the CN column difference between Run C and the base run in Figure 1b shows that the biggest increases by as much as 5×10^9 cm^{-2} occur in the tropics over the Atlantic Ocean. (Changes in cloud cover are reported in section 3.4.)

Table 1: Global-averaged values obtained from various model runs (for the period 2006–2010).

Model run	LNO_x (Tg N yr^{-1})	Tropospheric O_3 burden (Tg O_3)	Total/tropospheric O_3 column (DU)	CH_4 lifetime (yr)	CN column $\times 10^9$ (cm^{-2})
Run A (base)	4.8	271.8	304.6/27.8	7.61	7.419
Run B	4.8	276.0	304.8/28.2	7.55	7.409

Run C	6.9	303.7	308.4/30.9	6.97	7.919
Run D	6.9	294.3	307.2/30.0	7.17	7.577
Run E	6.9	303.6	308.2/30.9	6.97	7.918
Run F	0	214.8	296.0/22.3	9.26	6.546

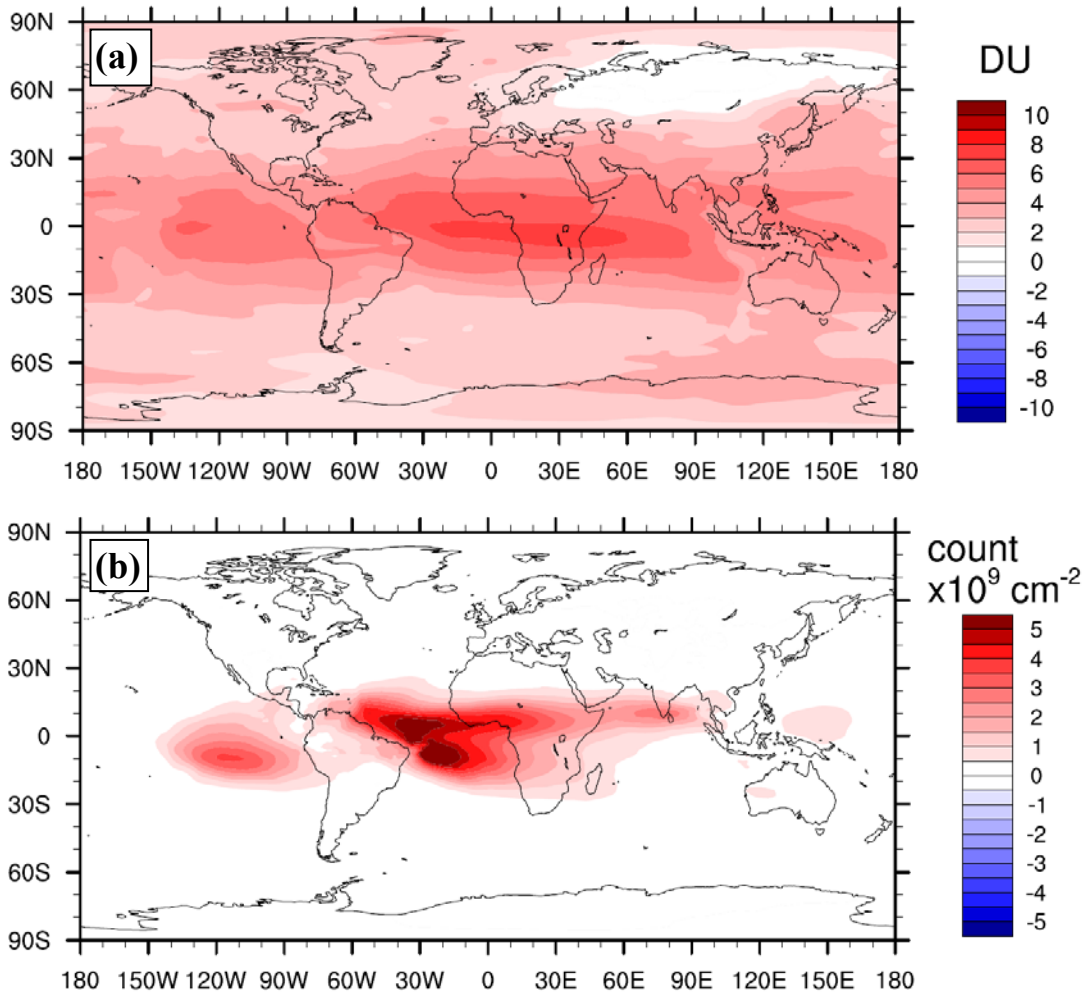

Figure 1: (a) Modelled column ozone difference (DU), and (b) column condensation nuclei (CN) concentration difference (× 10^9 count cm^{-2}) between Run C (i.e., the new dry deposition scheme and the new LNO_x scheme) and the base run (mean over 2006–2010).

3.2~~1~~ Model performance for all-sky radiative fluxes

Model output for radiative components for all-sky conditions includes the incoming (or downward) TOA solar radiation ($S\downarrow_{TOA}$) (which is the same in all model runs), outgoing (or upward) TOA longwave radiation ($L\uparrow_{TOA}$), outgoing TOA shortwave radiation ($S\uparrow_{TOA}$), incoming longwave radiation at the surface ($L\downarrow_{S}$), incoming shortwave radiation at the surface ($S\downarrow_{S}$), outgoing longwave radiation at the surface ($L\uparrow_{S}$), and outgoing shortwave radiation at the surface ($S\uparrow_{S}$). The total radiation is the sum of the longwave and shortwave components.

The net downward TOA radiative flux is

$$R^{N}_{TOA} = S\downarrow_{TOA} - (L\uparrow_{TOA} + S\uparrow_{TOA}), \quad (7)$$

where the superscript N signifies net (note that $S\downarrow_{TOA}$ is the same in all runs and $L\downarrow_{TOA} = 0$). Additional definitions are: the net downward TOA shortwave radiative flux $S^{N}_{TOA} = S\downarrow_{TOA} - S\uparrow_{TOA}$ and the net downward TOA longwave radiative flux $L^{N}_{TOA} = -L\uparrow_{TOA}$. The net downward longwave radiation at the surface (*rls*) is equal to ($L\downarrow_{S} - L\uparrow_{S}$) and net downward shortwave radiation at the surface (*rss*) is equal to ($S\downarrow_{S} - S\uparrow_{S}$). (Here the variable names in italics are based on standard CMIP convention used in model codes.) Table 2 gives a list of radiative flux symbols used. Model output for clear-sky $L\uparrow_{TOA}$ (*rlutcs*), $S\uparrow_{TOA}$ (*rsutcs*), $L\downarrow_{S}$ (*rldscs*), $S\downarrow_{S}$ (*rsdscs*) and $S\uparrow_{S}$ (*rsuscs*) was also available. Unless stated otherwise the reported radiative fluxes are for all-sky conditions.

Table 2: List of radiative flux symbols for all-sky conditions.

Symbol	Definition
$L\uparrow_{TOA}$	Outgoing (or upward) top-of-atmosphere longwave radiative flux (*rlut*)
$L\downarrow_{TOA}$	Incoming (or downward) top-of-atmosphere longwave radiative flux (= 0)
$S\downarrow_{TOA}$	Incoming top-of-atmosphere shortwave (or solar) radiative flux (*rsdt*)
$S\uparrow_{TOA}$	Outgoing top-of-atmosphere shortwave radiative flux (*rsut*)
$L\downarrow_{S}$	Incoming longwave radiative flux at the surface (*rlds*)
$S\downarrow_{S}$	Incoming shortwave radiative flux at the surface (*rsds*)
$L\uparrow_{S}$	Outgoing longwave radiative flux at the surface
$S\uparrow_{S}$	Outgoing shortwave radiative flux at the surface
R^{N}_{TOA}	Net downward top-of-atmosphere radiative flux ($= S^{N}_{TOA} + L^{N}_{TOA}$)
S^{N}_{TOA}	Net downward top-of-atmosphere shortwave radiative flux
L^{N}_{TOA}	Net downward top-of-atmosphere longwave radiative flux

In Table 3, the area-weighted globally-averaged modelled radiative fluxes~~The modelled radiation components~~ from the base ACCESS-UKCA run are in good agreement with the observed values~~can be compared with the corresponding observations~~ computed~~available~~ from NASA's Clouds and the Earth's Radiant Energy System (CERES) EBAF (Energy Balanced and Filled) Ed4.1 dataset (https://ceres.larc.nasa.gov/data/) for the period 2006–2010 (Loeb et al., 2018; Kato et al., 2018), and with ~~.~~those from a 16-model ensemble from CMIP5 twentieth-century experiments (Stephens et al., 2012) (the range in terms of model minimum and maximum values is given in parenthesis).

~~The area weighted global averaged modelled incoming $S\downarrow_{TOA}$, and all sky outgoing $L\uparrow_{TOA}$ and $S\uparrow_{TOA}$ radiative fluxes are 341.44, 240.61 and 102.24 W m^{-2}, respectively, in close agreement with the respective observed values of 339.93, 240.10 and 99.19 W m^{-2}. The modelled incoming $L\downarrow_S$ and $S\downarrow_S$ radiative fluxes are 341.55 and 191.49 W m^{-2} compared to the observed averages of 344.57 and 186.48 W m^{-2}, respectively. The modelled outgoing $L\uparrow_S$ and $S\uparrow_S$ radiative fluxes are 400.07 and 24.83 W m^{-2} compared to the observed averages of 398.18 and 23.21 W m^{-2}, respectively. Thus, the modelled average total net downward radiation at the surface is 108.14 W m^{-2} compared to the observed value of 109.66 W m^{-2}.~~

Table 3: Comparison of the modelled (base run) and observed radiative fluxes (W m^{-2}) for all-sky conditions. The values are global averages for the period 2006–2010 and the values in parenthesis are minimum and maximum values.

Radiative flux	Modelled	Observed	CMIP5
$S\downarrow_{TOA}$	341.44	339.93	343.0 (338.6–343.7)
$L\uparrow_{TOA}$	240.61	240.10	238.6 (232.4–243.5)
$S\uparrow_{TOA}$	102.24	99.19	102.2 (96.4–106.5)
$L\downarrow_S$	341.55	344.57	339.7 (326.4–347.0)
$S\downarrow_S$	191.49	186.48	190.3 (181.9–196.2)
$L\uparrow_S$	400.07	398.18	397.5 (391.9–398.1)
$S\uparrow_S$	24.83	23.21	24.9 (21.1–30.3)

~~The above values can also be compared with a 16-model ensemble from a CMIP5 study (Stephens et al., 2012), which gives the outgoing $L\uparrow_{TOA}$ and $S\uparrow_{TOA}$ of 238.6 and 102.2 W m^{-2}, respectively, and the incoming $L\downarrow_S$ and $S\downarrow_S$ of 339.7 and 190.3 W m^{-2}, respectively.~~

A comparison of the zonal-averaged modelled $L\uparrow_{TOA} + S\uparrow_{TOA}$, $L\downarrow_S$ and $S\downarrow_S$ with the corresponding CERES-EBAF data is made in Figure 4 and discussed in section 3.~~2~~3.

Fiddes et al. (2018) obtained similar evaluation results for a very similar setup of ACCESS-UKCA vn8.4 for radiation components averaged over the period of 2000–2009.

3.32 Radiative effects of the parameterisation changes

Figure 2a presents a bar charts of the modelled mean (2006–2010) difference (Δ) in the all-sky, area-weighted net downward TOA total radiation (ΔR^N_{TOA}) and its longwave (ΔL^N_{TOA}) and shortwave (ΔS^N_{TOA}) components between the various runs and the base run for the globe, tropics (here ≤< |30°|), extranon-tropics (> |30°|), land, and ocean (which includes all water bodies). In Figure 1, tThe absolute values of the total outgoing TOA radiative flux ($L\uparrow_{TOA}$ +$S\uparrow_{TOA}$), and $L\uparrow_{TOA}$ and $S\uparrow_{TOA}$ for the base run are also plotted as a reference (corresponding to the right y-axesis). Table 4 presents values of the differences ΔR^N_{TOA}, ΔL^N_{TOA}, ΔS^N_{TOA}, $\Delta L\downarrow_S$ and $\Delta S\downarrow_S$ for the globe, tropics, and extranon-tropics for all-sky conditions (Table S1 the Supplement gives additional modelled flux differences). ΔR^N_{TOA} is akin to radiative forcing; a positive ΔR^N_{TOA} means more radiation is retained in the atmosphere due to perturbation to the base model. It is apparent that with the new oceanic deposition scheme, the net downward TOA radiation (R^N_{TOA}) is increased, but by only a relatively very small amount of 4.43 mW m^{-2}. This small increase is due to an increase in the shortwave component which dominates over a decrease in the longwave component. With the new lightning flash-rate parameterisationscheme also included this is changeincrease in R^N_{TOA} is much greater at 86.3 mW m^{-2} as LNO_x increases to 6.9 from the base value 4.8 Tg N yr^{-1} with due to enhanced tropospheric O_3 production. This increase in R^N_{TOA} is due to an increase in both longwave and shortwave components, but the former dominates. Increased LNO_x causes enhanced OH concentrations resulting from the increased LNO_x that reduce the tropospheric CH_4 lifetime and would increase $L\uparrow_{TOA}$. and CH_4 loss. as LNO_x is increased (to 6.9 from the base value 4.8 Tg N yr^{-1}). If we turn off the radiative feedbacks of CH_4 in the model, the increase in R^N_{TOA} the net downward TOA radiative flux is 107.0 mW m^{-2}. In other words, the CH_4 feedback negates the positive radiative effect of O_3 feedback by 20.7 mW m^{-2};. (Note that dry deposition is a surface process and, therefore, any changes to it would influence O_3 in surface air to much greater extent than that at higher altitudes, soalthough the radiative effects of these changes may be very small.)

When the default PR92 lightning flash--rate scheme is used with a uniform global scaling (by a factor of 1.44) so as to give the total global LNO_x the same as that obtained by Run C3 with the new lightning flash-rate scheme (i.e., 6.9 Tg N yr^{-1}), the increase in R^N_{TOA} the net downward TOA radiation is 70.9 mW m^{-2}. As stated earlier, while the PR92 scheme for land performs very similar to the new scheme in simulating the global spatial distribution of lightning flash rate over land, the oceanic PR92 scheme underestimates the global mean flash-rate distribution considerably over the ocean. Therefore, this uniform scaling of the PR92-derived global flash-rate distribution would cause an over-adjustment of the flash rate (and hence LNO_x) over land to compensate for the underestimation by the oceanic parameterisation. Therefore, although the total global LNO_x is the same in both Rruns C and D, there is a mismatch in its spatial distribution with Run D having larger LNO_x over land and continue to have lower LNO_x over the ocean than Run C. Thus, the new lightning flash--rate scheme leadings to a larger increase in R^N_{TOA} than that obtained by the scaled PR92 scheme, which implies that how LNO_x is spatially distributed makes a difference in the radiation impact. This difference could possibly be because adding LNO_x to the lower NO_x levels in the marine upper

troposphere causes greater ozone production than adding it to the NO_x richer continental upper troposphere, and also because of differences in the photochemical reaction rates as a result of temperature differences over land and sea.

~~LNO_x is an important precursor of tropospheric O_3 and OH.~~ Turning off LNO_x completely in the model causes an extra 190.8 mW m^{-2} to leave the atmosphere compared to the base run. This relates to~~is caused by~~ the lower amount of O_3 due to the absence of LNO_x in the atmosphere. This increase in outgoing radiation related ~~due~~ to the reduced upper tropospheric O_3 dominates over the reverse radiative~~on~~ impact of no LNO_x causing lower OH and hence a longer CH_4 lifetime.

In Figure 2a, the all-sky radiation changes relative to the base run are larger in magnitude in the tropics than elsewhere. With the new oceanic deposition scheme, the net downward TOA radiation is increased by 13.7 mW m^{-2} in the tropics but is reduced by 5.5 mW m^{-2} elsewhere. The contrast in radiation changes over land and~~the~~ ocean is not as stark as that over the tropical and extra~~non~~-tropical regions, except for the no-LNO_x case.

Figure 2b and Figure 2c are the same as Figure 2a except that they are for the differences in the net downward TOA radiation components L^N_{TOA} and S^N_{TOA}, respectively~~,~~ (Table 4 gives the values). ~~and t~~These plots suggest that when the new LNO_x scheme is used, the changes in the total net downward TOA radiation are dominated by the changes in the longwave component (L^N_{TOA}).

~~The magnitude of the above modelled net downward TOA radiation differences obtained due to the differences in the representation of two natural processes in the model can be put in the context of the IPCC AR6 reported anthropogenic ERF due to O_3 over the years 1750–2019 of 470 ± 230 mW m^{-2} (Forster et al., 2021), noting that the radiation differences calculated here are akin to instantaneous radiative forcing, which excludes any adjustments (e.g., adjustments causing circulation changes) unlike the ERF which is the sum of the IRF and the contribution from the adjustments. For example, the extra radiation of 86.3 mW m^{-2} retained by the atmosphere when the new deposition and lightning flash rate schemes are used, which represents the uncertainty in radiation due to two natural process representation in chemistry-climate models, is 18% of the anthropogenic O_3 radiative forcing.~~

Figure 3a is a bar chart of the modelled mean difference of the area-weighted downward surface longwave radiative flux ($\Delta L{\downarrow}_S$) between the various runs and the base run. The absolute values of the surface longwave radiative flux for the base run are also plotted as a reference. Figure 3b is the corresponding plot for the downward surface shortwave radiative flux difference ($\Delta S{\downarrow}_S$). The LNO_x increases in the model, compared to the base run, lead to an increase in $L{\downarrow}_S$, and a decrease in $S{\downarrow}_S$.

Table 4 also presents the mean global radiative flux differences for clear-sky conditions (Table S2 in the Supplement gives additional clear-sky modelled flux differences). For the case when the new deposition and lightning flash-rate parameterisations are used, the clear-sky ΔR^N_{TOA} is greater at 110.8 mW m^{-2} compared to the all-sky value of 86.3 mW m^{-2}, and in both cases this change is dominated by the longwave component. For the case when only the new ozone dry deposition scheme is used, the clear-sky ΔR^N_{TOA} is again relatively very small at -6 mW m^{-2} (driven by a decrease in the longwave component) but is in opposite direction compared to the corresponding all-sky case. The clear-sky mean global increases in

the surface $L\downarrow_S$ are larger compared to the all-sky increases. Thus, while the all-sky and clear-sky radiations show qualitatively similar changes in response to changes in LNO_x, the differences in the magnitude of these changes imply an impact of LNO_x on clouds and an analysis on this is given in section 3.4.

Table 4: Changes in the modelled net downward total TOA radiative flux (ΔR^N_{TOA}), net downward TOA longwave radiative flux (ΔL^N_{TOA}), net downward TOA shortwave radiative flux (ΔS^N_{TOA}), and incoming longwave ($\Delta L\downarrow_S$) and shortwave ($\Delta S\downarrow_S$) radiative fluxes at the surface, with respect to the base model run. Values (mW m^{-2}) are averages over 2006–2010.

Region	Parameter	Model difference from base run (mW m^{-2})				
		1 (dep.)	2 (dep. + LNO_x)	3 (dep. + scaled LNO_x)	4 (dep. + LNO_x + no CH_4)	5 (dep. + no LNO_x)
Globe (all sky)	ΔR^N_{TOA}	4.4	86.3	70.9	107.0	-190.8
	ΔL^N_{TOA}	-2.5	74.0	54.8	101.2	-184.3
	ΔS^N_{TOA}	6.9	12.3	16.1	5.8	-6.5
	$\Delta L\downarrow_S$	9.0	93.1	69.7	92.3	-199.2
	$\Delta S\downarrow_S$	7.8	-72.1	-44.6	-75.6	204.9
Tropics (all sky)	ΔR^N_{TOA}	13.7	133.4	113.0	163.2	-264.8
	ΔL^N_{TOA}	1.2	115.8	82.7	149.3	-266.2
	ΔS^N_{TOA}	12.5	17.6	30.3	13.9	1.4
	$\Delta L\downarrow_S$	4.7	131.0	90.5	135.1	-283.7
	$\Delta S\downarrow_S$	17.7	-95.3	-49.5	-98.4	266.3
Extra-tropics (all sky)	ΔR^N_{TOA}	-5.5	37.4	27.1	48.6	-114.1
	ΔL^N_{TOA}	-6.5	30.5	25.8	51.1	-99.4
	ΔS^N_{TOA}	1.0	6.9	1.3	-2.5	-14.7
	$\Delta L\downarrow_S$	13.4	53.8	48.2	47.9	-111.4
	$\Delta S\downarrow_S$	-2.4	-47.9	-39.5	-51.9	141.1
Globe (clear sky)	ΔR^N_{TOA}	-6.0	110.8	77.6	132.9	-276.5
	ΔL^N_{TOA}	-7.4	95.2	69.2	123.0	-245.2
	ΔS^N_{TOA}	1.4	15.6	8.4	9.9	-31.3
	$\Delta L\downarrow_S$	21.9	143.7	106.9	145.2	-287.3
	$\Delta S\downarrow_S$	-0.2	-70.0	-54.3	-72.8	177.4

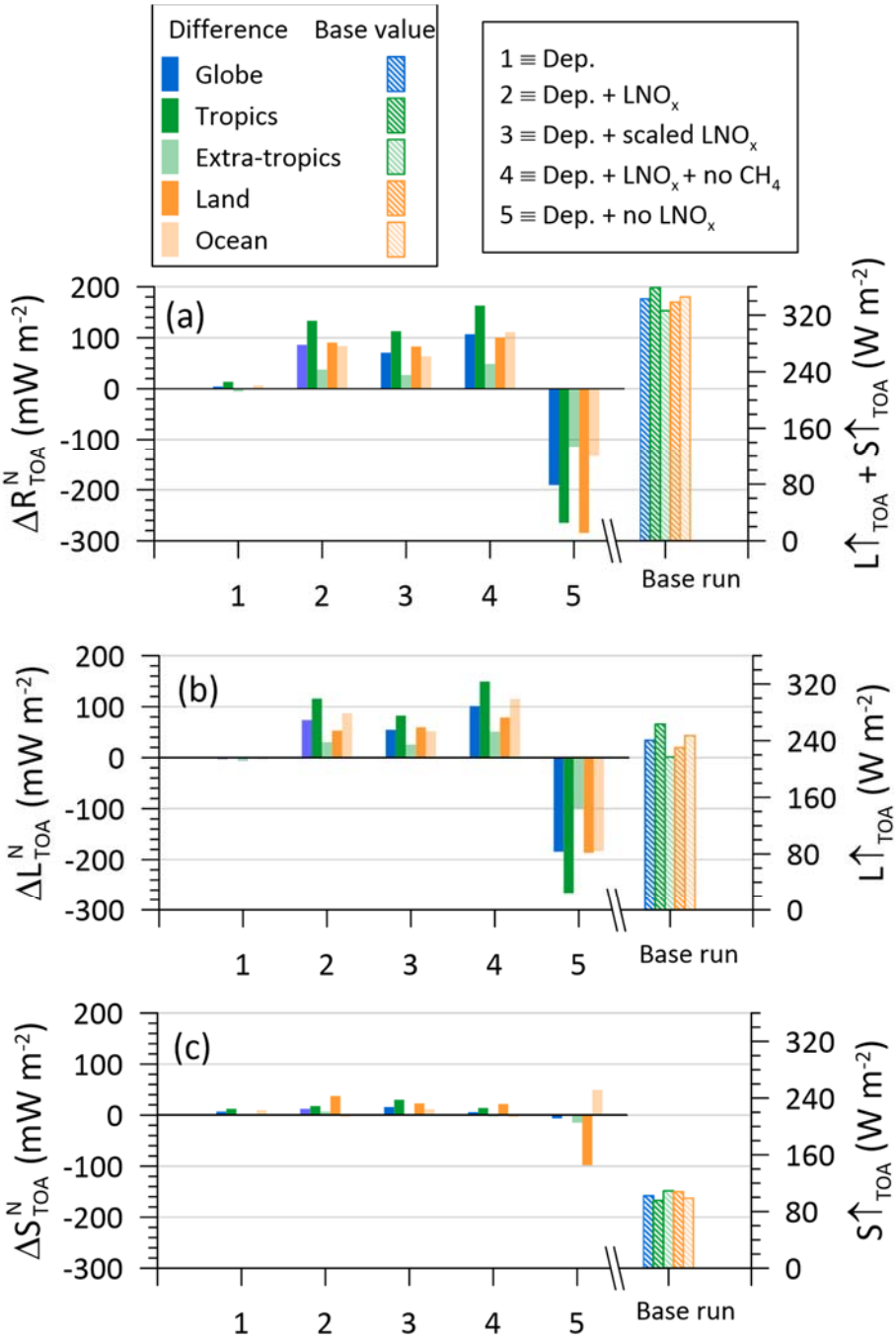

Figure 2: Modelled mean (2006–2010) all-sky net downward TOA radiative flux difference between the various model runs and the base run (1 = Run B – Base, 2 = Run C – Base, 3 = Run D – Base, 4 = Run E – Base, 5 = Run F – Base) for the globe, tropics ~~(< |30°|)~~, extra~~non~~-tropics, land, and ocean. The plots are for the (a) total radiative flux difference (ΔR^N_{TOA}), (b) longwave radiative flux difference (L^N_{TOA}), and (c) shortwave radiative flux difference (S^N_{TOA}). The outgoing TOA flux values obtained from the base run are also plotted (corresponding to the right y-axis).

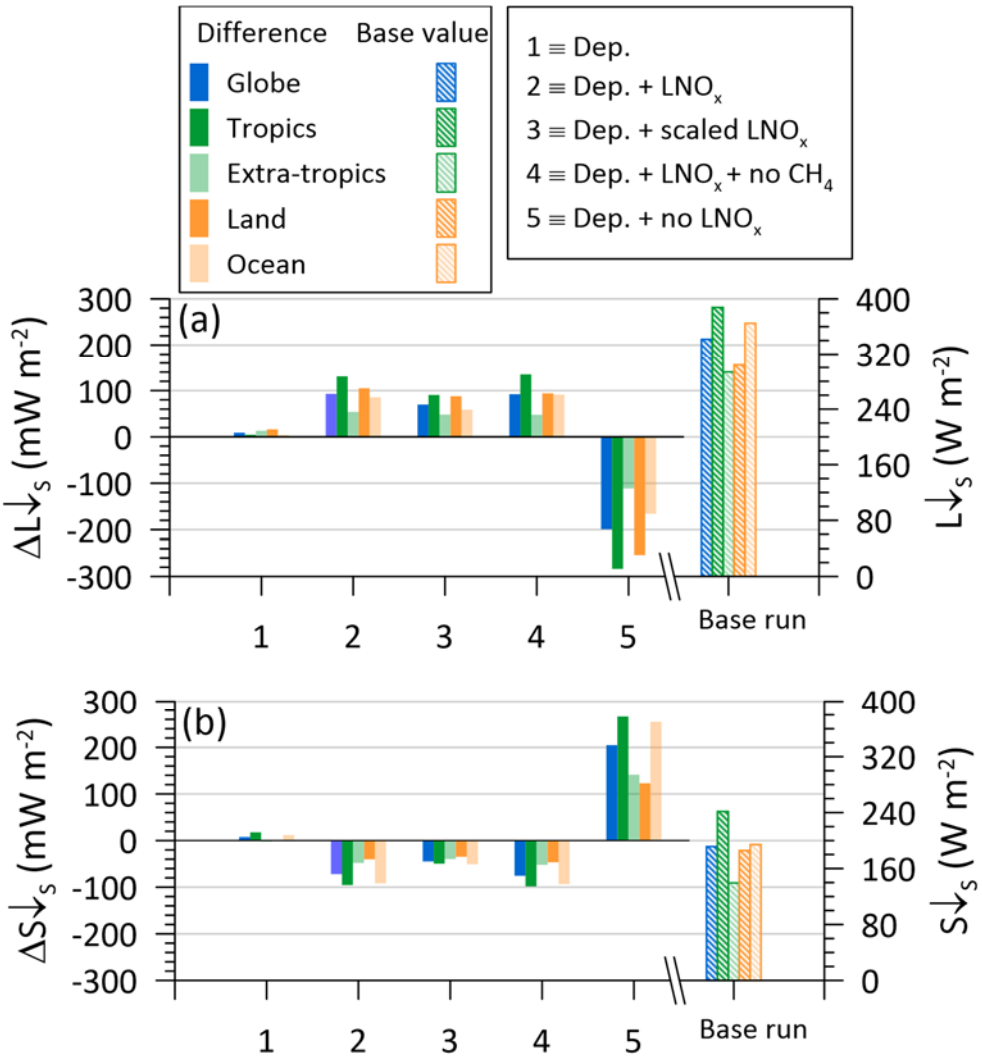

Figure 3: Modelled mean (2006–2010) all-sky downward surface radiative flux difference between the various model runs and the base run (1 = Run B – Base, 2 = Run C – Base, 3 = Run D – Base, 4 = Run E – Base, 5 = Run F – Base) for the globe, tropics ~~(< |30°|)~~, extra~~non~~-tropics, land, and sea. The plots are for the (a) longwave radiative flux difference ($\Delta L\downarrow_S$) and (b) shortwave radiative flux difference ($\Delta S\downarrow_S$). The downward surface flux ($L\downarrow_S+S\downarrow_S$) values obtained from the base run are also plotted (corresponding to the right y-axis).

In Figure 4 (a, b and c), the variations of the modelled zonal means ~~means~~of ~~the differences~~ ΔR^{N}_{TOA}, ~~in the modelled radiative fluxes from the base model run for the various other model runs for downward TOA net radiative flux, downward surface longwave radiative flux~~ $\Delta L\downarrow_S$ and ~~downward surface shortwave radiative flux~~ $\Delta S\downarrow_S$ are presented (solid lines). The zonal means~~means~~ of the absolute total outgoing TOA radiative flux ($L\uparrow_{TOA}$ +$S\uparrow_{TOA}$), $L\downarrow_S$ and ~~downward long wave radiative flux at the surface and downward short wave radiative flux at the surface~~ $S\downarrow_S$ obtained from the base run~~, and the corresponding CERES-EBAF data,~~ are also plotted and compared with the corresponding CERES-EBAF data (dotted lines and solid circles, corresponding to the right y-axis).

In Figure 4a, the minimum in the ~~zonal mean of the~~ modelled $L\uparrow_{TOA}$ +$S\uparrow_{TOA}$ ~~flux~~ near the equator is mostly due to the high cloud tops associated with the inter-tropical convergence zone (ITCZ), which is a region of persistent thunderstorms, and the subtropical maxima are associated with clear air over deserts and subtropical highs. The radiative flux diminishes towards the poles, with the minimum being in the southern hemisphere polar region. There is a good agreement with the CERES-EBAF data, with some model overestimation between 50°N to 50°S and underestimation within 50–70°S. Looking at the ~~In terms of the~~ differences ΔR^{N}_{TOA} ~~in net downward total top of the atmosphere (TOA) radiative flux () from the base run~~, dry deposition has little effect, but increased LNO_x increases the flux from ~ 50°N to 30°S presumably due to increased emission of LW by O_3 produced by the LNO_x. Similarly, totally removing the LNO_x decreases the TOA radiative flux particularly from approximately 30°S to virtually the north pole showing a marked hemispheric asymmetry towards the northern hemisphere. This contrasts, being in the opposite hemisphere, to the asymmetric effect of LNO_x on the downward SW radiation at the surface (Figure 4c).

The radiative flux ~~Downwards longwave radiation at the surface~~e ~~in clear sky conditions is such that 80% originates in the first 500 m of the atmosphere and the major controlling factors~~ $L\downarrow_S$ primarily depends on~~are~~ water vapour~~humidity~~ and temperature in the lower atmosphere and varies with increasing CO_2 and other greenhouse gases (Wang and Dickinson, 2013), including O_3 (Rap et al., 2015). In Figure 4b~~, for~~ $L\downarrow_S$~~downward long wave radiative flux at the surface~~ has a ~~, apparent are the~~ characteristic peak in the tropics~~,~~ and it ~~the radiative flux~~ diminish~~es~~ing poleward to a lower level in the northern polar region and to the lowest levels towards the southern hemisphere pole consistent with global climatologies (Wang and Dickinson, 2013). The model agreement with the CERES-EBAF data is excellent. In terms of $\Delta L\downarrow_S$~~the differences from the base run~~, dry deposition has little effect, but increased LNO_x increases the downward flux from ~ 40°N to 40°S presumably due to increased emission of LW by O_3 produced by the LNO_x. Similarly, totally removing the LNO_x decreases LW radiation particularly from ~ 40°N to 40°S. This contrasts with the asymmetric effect of LNO_x on SW radiation in Figure 4c.

The ~~downward short wave~~ radiative flux ~~at the surface~~$S\downarrow_S$ is affected by clouds which reflect and scatter solar radiation (see cloud climatology https://earthobservatory.nasa.gov/images/85843/cloudy-earth). In Figure 4c for $S\downarrow_S$~~downward shortwave~~

~~radiative flux at the surface~~, apparent are the characteristic peak from overhead solar radiation in the tropics, the influence of the tropical cloud band, the radiative flux diminishing to a low level in the northern polar region presumably due to widespread cloud cover there, and diminishing fluxes in the mid latitudes of the southern hemisphere and then increasing towards the pole consistent with cloud climatologies (https://earthobservatory.nasa.gov/images/85843/cloudy-earth). The model agreement with the CERES-EBAF data is good, with some model overestimation in the tropics. Considering~~In terms of~~ the difference $\Delta S\downarrow_S$~~the differences from the base run~~, dry deposition has little effect, but increased LNO_x decreases the downward flux from ~ 20°N to 60°S~~presumably due to increased absorption of SW by O_3 produced by the LNO_x~~. Similarly, totally removing the LNO_x increases SW radiation from ~ 40°N to 70°S, which~~This~~ illustrates the asymmetric effect of LNO_x ~~in producing O_3~~ across the hemispheres (and consequent asymmetric heating contribution). Generally, most of the SW radiation in the wavelength spectrum that O_3 can efficiently absorb is removed by the stratospheric O_3 such that little penetrates to the Earth's surface (Rap et al., 2015). Therefore, the decrease in $S\downarrow_S$ with LNO_x is possibly not directly caused by the increased O_3 production as a result of the increased LNO_x, but could instead be driven by other factors such as changes in aerosol or cloud between the perturbed parameterisation experiments and the base run in response to changes in LNO_x. We have explored this in the next section.

Global distribution of the ~~net downward TOA radiative flux~~ difference ~~(~~ΔR^N_{TOA}~~)~~ between the model Run C (i.e., the new dry deposition scheme and the new LNO_x scheme; Diff. 2) and the base run (Figure 5a) is patchy with regions of both increased and decreased radiation compared to the base run, but with an overall increase. The difference in the incoming longwave radiative flux at the surface ($\Delta L\downarrow_S$) (Figure 5b) is positive almost everywhere over the globe, whereas that in the incoming shortwave radiative flux at the surface ($\Delta S\downarrow_S$) (Figure 5c) has a patchy global distribution with regions of both positive and negative values. The respective area-weighted global spatial means of these differences in Figure 5a, b and c are 86.3 ± 387.3, 93.1 ± 184.1 and -72.1 ± 589.9 mW m^{-2}, where the standard deviations were obtained from area-weighted variances and their relatively large values reflect the spatial heterogeneity of the radiation response.

Figure 5d presents the corresponding difference in lightning flash density (Δf) between the two models, which shows a larger flash density predicted everywhere by the new LNO_x scheme, particularly over the ocean in the tropics (LNO_x is directly proportional to the lightning flash rate in our model). The area-weighted spatial pattern correlation (r) between Δf and ΔR^N_{TOA} is 0.15. The correlation of Δf with $\Delta L\downarrow_S$ is 0.33 and with $\Delta S\downarrow_S$ it is -0.14. These relatively low correlations imply that while the LNO_x production occurs (and changes from model run to run) in one spatial pattern, time is required for chemical processing from NO_x to O_3 and CH_4 and during this time advection and dispersion take place, and also the feedbacks from the impact on aerosol and cloud cover, so that the radiative effects occur in a different spatial pattern compared to the lightning flash rate. The area-weighted spatial pattern correlations between the difference in the ozone column (ΔDU) in Figure 1, and ΔR^N_{TOA}, $\Delta L\downarrow_S$ and $\Delta S\downarrow_S$ are 0.24, 0.48 and -0.14, respectively.

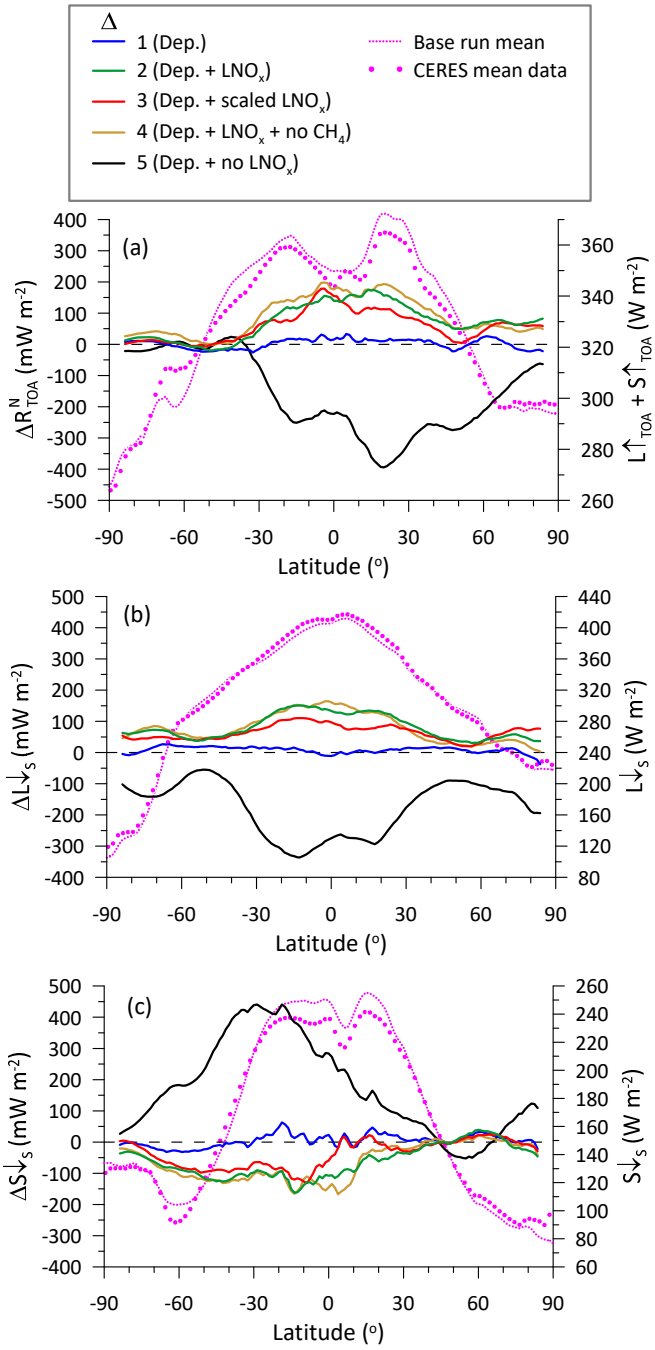

Figure 4: Zonal mean (2006–2010) of all-sky radiative flux difference between the various model runs and the base run (1 = Run B – Base, 2 = Run C – Base, 3 = Run D – Base, 4 = Run E – Base, 5 = Run F – Base). The plots (solid lines) are for the (a) net downward TOA radiative flux difference (ΔR^N_{TOA}), (b) downward longwave radiative flux difference at the surface ($\Delta L\downarrow_S$) and (b) downward shortwave radiative flux difference at the surface ($\Delta S\downarrow_S$). The solid lines are running averages (over a moving window of 10 points, i.e., 12.5°). The zonal mean flux values obtained from the base run and the corresponding CERES-EBAF data are also plotted (dotted line and solid circles, corresponding to the right y-axis).

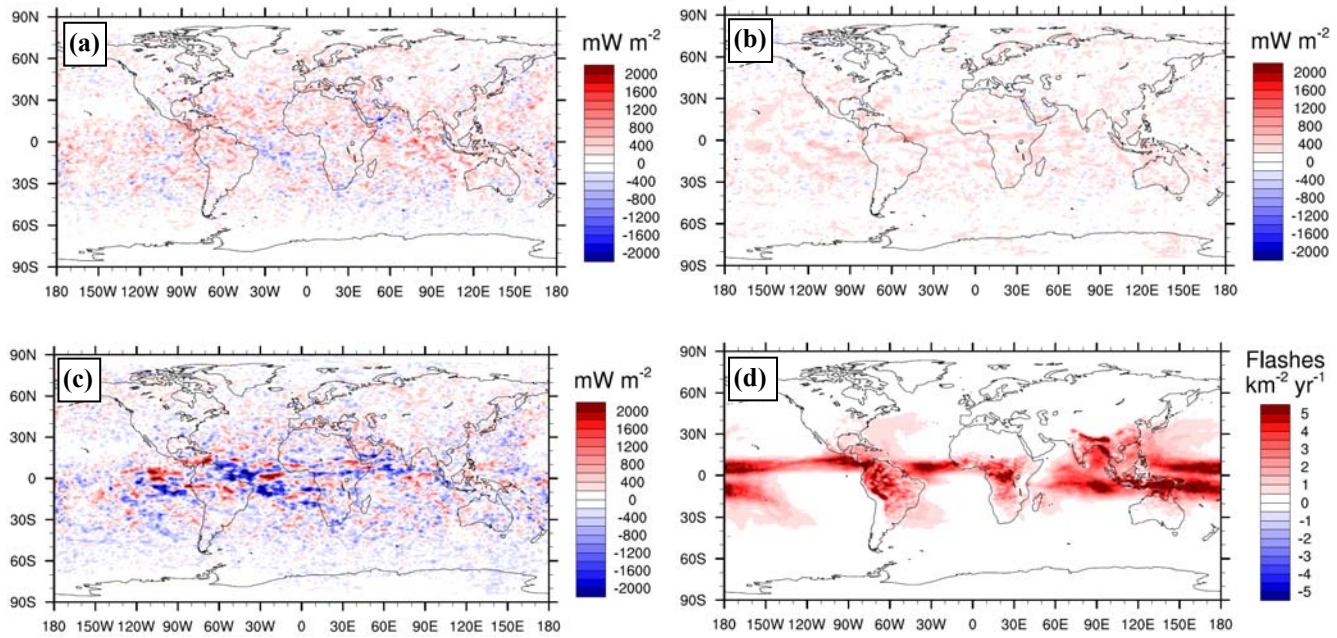

Figure 5: Global distribution of the all-sky radiative flux difference (mW m^{-2}) between Run C (i.e., the new dry deposition scheme and the new LNO$_x$ scheme) and the base run (mean over 2006–2010). The plots are for the (a) net downward TOA radiative flux difference (ΔR^{N}_{TOA}), (b) incoming longwave radiative flux difference at the surface ($\Delta L{\downarrow}_S$) and (~~b~~c) incoming shortwave radiative flux difference at the surface ($\Delta S{\downarrow}_S$). In (d), the corresponding model difference in lightning flash density, given as flashes km^{-2} yr^{-1}, is shown.

3.4 Changes in incoming surface shortwave radiation, aerosol and cloud cover

As stated earlier, the decrease in all-sky $S{\downarrow}_S$ cannot not be explained by the increased O_3 production as LNO_x is increased, and therefore to further understand what drives the differences in the shortwave flux at the surface we look at any changes in aerosol fields and cloud cover that may explain this decrease. We only consider the parameter value differences between the model run with both the new oceanic O_3 dry deposition scheme and the new lightning flash-rate parameterisation (Run C) and the base model run, and the zonal means of these differences are shown in Figure 6. The increased LNO_x in Run C also leads to a decrease in the clear-sky $\Delta S{\downarrow}_S$ and this corresponds to an increase in the column integrated CN (or aerosol) number concentration. Increases in the column integrated CN by as much as 2×10^9 cm^{-2} are found. These aerosol in addition to reflecting and scattering solar radiation, also affect clouds. The all-sky $\Delta S{\downarrow}_S$ is more asymmetric across the hemispheres than the clear-sky $\Delta S{\downarrow}_S$, which could be due to the hemispheric asymmetric in ΔCN coupled with influence of changes in cloud properties.

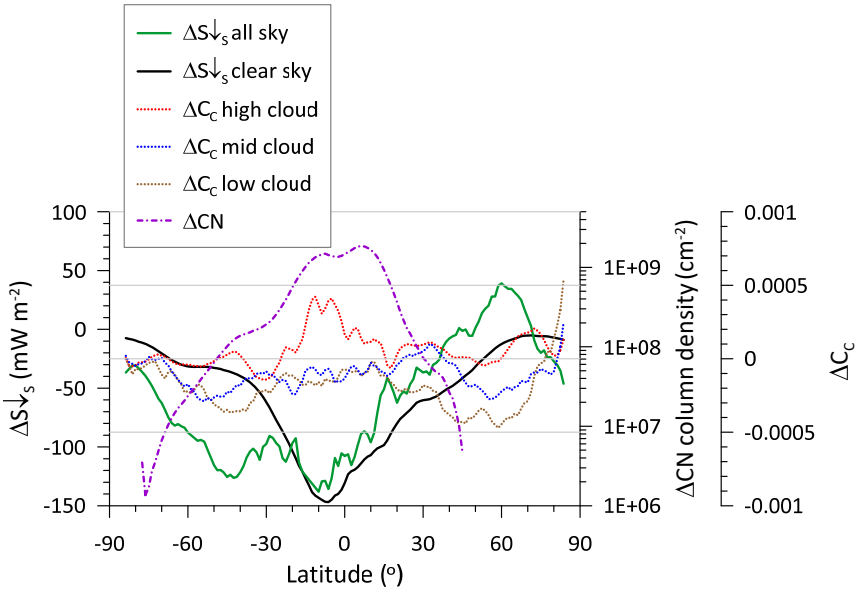

Figure 6: Zonal mean (2006–2010) of parameter value differences between the model run with both the new oceanic O_3 dry deposition scheme and the new lightning flash-rate parameterisation and the base model run (Run C – Base): all-sky downward shortwave radiative flux difference at the surface ($\Delta S\downarrow_S$); clear-sky $\Delta S\downarrow_S$; differences in high, medium and low cloud cover (ΔC_C); and column integrated condensation nuclei (CN) concentration difference (ΔCN). The lines are running averages (over a moving window of 10 points, i.e., 12.5°).

We also calculated changes in cloud cover C_C (or cloud fraction, which varies between 0–1) for low (< 2 km), middle (2–6 km) and high (> 6 km) level clouds. Cloud cover is important for the modelling of downward radiation (Chen et al., 2012), and the model output for this quantity was available for each grid box at each model level. The total cloud cover within the above three cloud-height categories can be calculated approximately from the modelled cloud cover at each model layer using a cloud overlap assumption. We used the combined maximum/random cloud overlap assumption which lies between the random overlap assumption (which overestimates the total cloud cover) and the maximum overlap assumption (which underestimates the cloud cover) (Oreopoulos and Khairoutdinov, 2003). Figure 6 shows the zonal means of cloud cover differences (ΔC_C) between Run C and the base model run for the high, middle, and low level clouds. It is apparent that cloud cover is impacted at all levels by the model changes, with more high-level and less middle- and low-level cloud cover, although the degree of changes being small, all within ± 0.05%. The high-level zonal mean ΔC_C appears to be noticeably anti-correlated with all-sky zonal mean $\Delta S\downarrow_S$ in the tropics whereas for northern latitudes above about 40° both middle- and low-level zonal mean ΔC_C are anti-correlated with $\Delta S\downarrow_S$.

Figure 7 presents the global spatial distributions of ΔC_C for the three cloud-height categories, which are patchy with regions of both positive and negative values. But visually comparing Figure 7a for the high-level cloud cover with the all-sky $\Delta S\downarrow_S$

global distribution in Figure 5c, one can clearly notice that regions of $\Delta S\downarrow_S$ are anticorrelated with ΔC_C, and that this anticorrelation becomes progressively weaker for middle- and low-level ΔC_C in Figure 7b and Figure 7c, respectively. The area-weighted spatial pattern correlation between $\Delta S\downarrow_S$ and ΔC_C is -0.44, -0.39, and -0.30 for the high-, middle-, and low-level cloud, respectively.

The above results suggest that while the decrease in the all-sky $\Delta S\downarrow_S$ with increased LNO_x may not possibly be explained in terms of the consequent O_3 production, the indirect effect of LNO_x on aerosol and cloud can at least partly explain the differences in the shortwave flux at the surface.

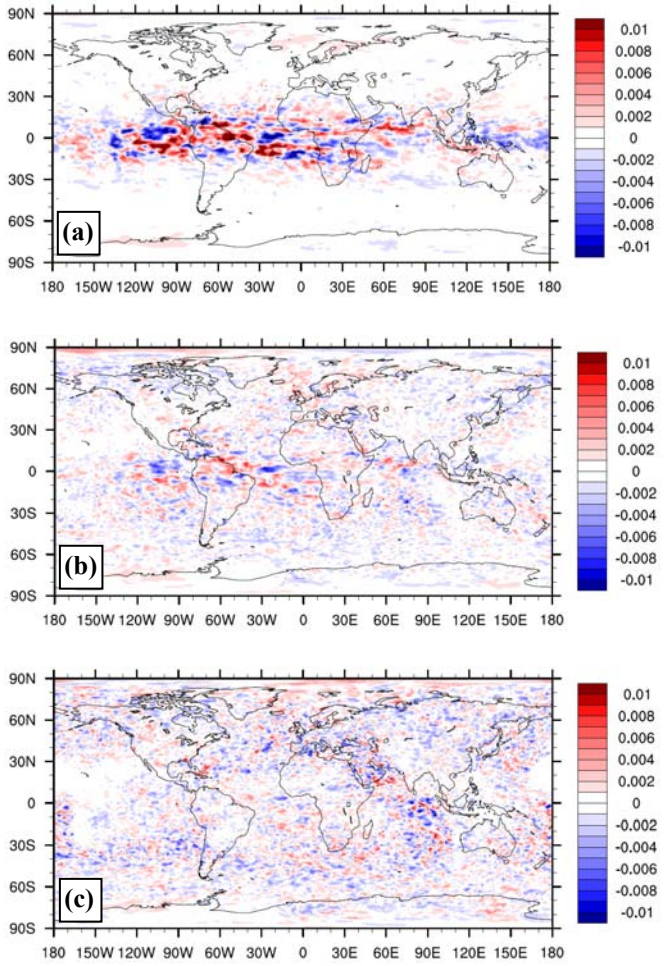

Figure 7: Global distribution of the modelled cloud cover (or cloud fraction) difference (ΔC_C) between Run C (i.e., the new dry deposition scheme and the new LNO_x scheme) and the base run (mean over 2006–2010). The plots are for (a) high level (> 6 km), (b) middle level (2–6 km) and (c) low level (< 2 km) clouds.

3.53 Radiative effects as a function of changes in LNO_x

Lightning NO_x production is a natural process with effects on the atmospheric radiation and energy budget via O_3, CH_4, and ~~nitrate~~ aerosol. Lightning NO_x is different from the bulk of other natural and anthropogenic sources of NO_x in the troposphere in that the release occurs in the upper portion of the troposphere rather than close to the Earth's surface.

In Figure 8a, we plot the change in the modelled net downward total TOA radiation (ΔR^{N}_{TOA}) as a function of change in the annual-averaged LNO_x production relative to the base model run. The different points are for different years and different model runs. All runs except Run E (i.e., without the CH_4 radiation feedback) are considered. The plot shows an approximately linear increasing change in the net downward total TOA radiation as a function of increase in the LNO_x production due to the various model parameterisation/configuration changes considered. (There is a relatively large gap between the LNO_x = 0 case and the LNO_x = 4.8 Tg N yr^{-1} case. To confirm that the linear fit is not unduly dominated by the LNO_x = 0 case and that the linearity is appropriate, an additional model simulation the same as Run C but with the LNO_x distribution scaled uniformly by 0.35 to give an averaged total LNO_x = 2.4 Tg N yr^{-1} was made, and the results from ~~the~~ this simulation are also plotted in Figure 8–Figure 9 enclosed by a dotted circle and they are included in determining the linear fits.)

The slope of the best fit lines in Figure 8a suggests that with a per Tg increase in N production per year due to lightning, there is an increase of 39.6 mW m^{-2} (Tg N yr^{-1})$^{-1}$ in the net downward TOA radiation, or that much of radiation is retained by the atmosphere. Similarly, based on the slopes of the best fit lines in Figure 8b and Figure 8c, there is an increase of 40.2 mW m^{-2} (Tg N yr^{-1})$^{-1}$ in the incoming surface longwave radiation, and a decrease of 36.4 mW m^{-2} (Tg N yr^{-1})$^{-1}$ in the incoming surface shortwave radiation.

~~Assuming an uncertainty range of 2–8 Tg N yr^{-1} in the global estimates of lightning generated NO_x suggested by Schumann and Huntrieser (2007), the uncertainty range in the net downward TOA radiation retained in the atmosphere due to uncertainty in LNO_x could thus be as much as 237.6 mW m^{-2} (recall that this is the net or combined radiative effect of positive O_3 and negative CH_4 feedbacks). Although these cannot be compared directly, this is equivalent to 50% of the present day anthropogenic ERF of 470 mW m^{-2} due to O_3 over the years 1750–2019 reported by IPCC AR6 (Forster et al., 2021). The corresponding uncertainty range is 241.2 mW m^{-2} for the surface longwave radiation and 218.4 mW m^{-2} for the surface shortwave radiation. Thus, the implications of this uncertainty in LNO_x for global climate modelling needs investigation and clarification.~~

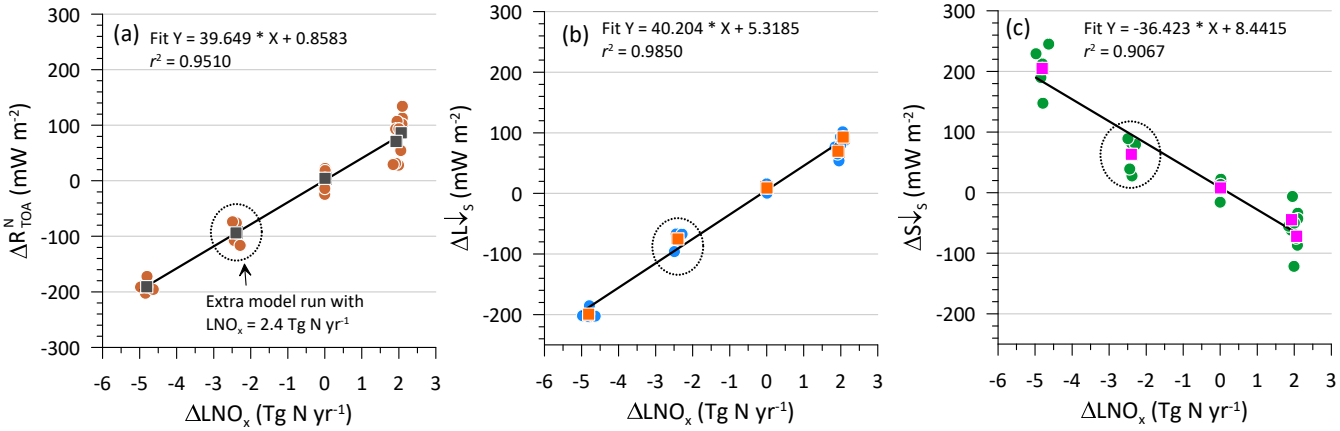

Figure 8: Change in the modelled (a) net downward total TOA radiation (ΔR^N_{TOA}), (b) incoming surface longwave radiation ($\Delta L\downarrow_S$), and (c) incoming surface shortwave radiation ($\Delta S\downarrow_S$), as a function of change in the modelled lightning-generated NO_x (ΔLNO_x, Tg N per year) relative to the Base model run. All runs except Run E (i.e., without the CH_4 radiation feedback) are considered. Results from an additional model simulation the same as Run C but with averaged LNO_x = 2.4 Tg N yr^{-1} are also plotted (enclosed in a dotted circle) to check linearity. The solid circles are the annual means whereas the squares are the mean over 2006–2010. The best fit line is based on all points.

~~The emission-based ERF due to increases in anthropogenic NO_x emissions (from 1750 to 2019) based on chemistry-climate models is reported to be negative (at -0.29 ± 0.29 W m^{-2}), which is a net effect of a positive ERF through enhanced tropospheric O_3 production, a negative ERF through reduced CH_4 lifetime, and a small negative ERF contribution through formation of nitrate aerosols (Naik et al., 2021). As demonstrated in this study, the net instantaneous radiative forcing of LNO_x is positive as the enhanced O_3 production dominates over the reduced CH_4 lifetime. Notwithstanding the differences between ERF and IRF, this could at least be partially because (a) in the upper to middle troposphere within which LNO_x is generated, the production efficiency of O_3 per unit of NO_x is much larger than that close to the Earth's surface, where anthropogenic emissions are mostly released (Dahlmann et al., 2011) and (b) the historical anthropogenic NO_x emissions were accompanied by emissions of reactive VOCs which affects the subsequent chemistry.~~

3.~~6~~4 Radiative effects as a function of changes in column O_3

~~With the new dry deposition scheme, the tropospheric O_3 burden increases by 1.5% (by 4.2 Tg O_3 from 271.8 Tg O_3) over the base run. With both the new dry deposition and LNO_x schemes this increase in the tropospheric O_3 burden is by 11.7%. Similarly, the increase in the O_3 column is by 0.14 DU for the new dry deposition scheme and 3.75 DU for the new dry deposition and LNO_x schemes combined (from the base average total column of 304.64 DU, and the base average tropospheric column of 27.82 DU).~~

Radiation is examined with respect to ~~tropospheric~~ O_3 column changes (Figure 9) caused by the dry deposition and LNO_x parameterisation changes. Based on Figure 9a, with a per DU increase in O_3, there is an increase of 22.8 mW m^{-2} DU^{-1} in the net downward TOA radiation, when the O_3 change is dominated by an increase in LNO_x. This can be compared to normalised

radiative forcing calculations reported in the scientific literature. Using the results of 17 atmospheric chemistry models, Stevenson et al. (2013) derived a globally averaged normalized radiative forcing of 42 (range 36–45) mW m^{-2} DU^{-1} for tropospheric O_3 increase from preindustrial (1750) to present day (2010). Gauss et al. (2003) calculated a normalized radiative forcing of 36 ± 3 mW m^{-2} DU^{-1} due to changes in tropospheric O_3 between 2000 and 2100 based on the results of 11 models. In our study, the changes in TOA radiative effects per DU, which are primarily driven by changes in the LNO_x parameterisation and to a much lesser extend by the O_3 deposition parameterisation (with CH_4 feedbacks included), are about half the radiative forcing per DU as a result of climate-scale changes in tropospheric O_3 (e.g., due to changes in precursor emissions and temperature). The climate-scale changes in radiation due to O_3 are larger, possibly because there are co-emissions of non-NO_x precursor species (e.g., CH_4 and VOCs) and their feedbacks, whereas in the present case only LNO_x and O_3 dry deposition changes are considered (together with CH_4 feedbacks). Methane levels and VOC emissions are unchanged. In any event, a clear distinction should be made between the expected column ozone changes arising from a change in LNO_x emissions versus a change in anthropogenic NO_x emissions.

Similarly, based on Figure 9b and Figure 9c, there is an increase in downward surface longwave radiation $L{\downarrow}_S$ by 23.6 mW m^{-2} DU^{-1} and a decrease in downward surface shortwave radiation $S{\downarrow}_S$ by 21.7 mW m^{-2} DU^{-1}. (As discussed earlier, changes in $S{\downarrow}_S$ can be explained in part by changes in aerosol fields and cloud cover as LNO_x is increased, but it is clear here that there is a good statistical correlation between $\Delta S{\downarrow}_S$ and ΔDU).

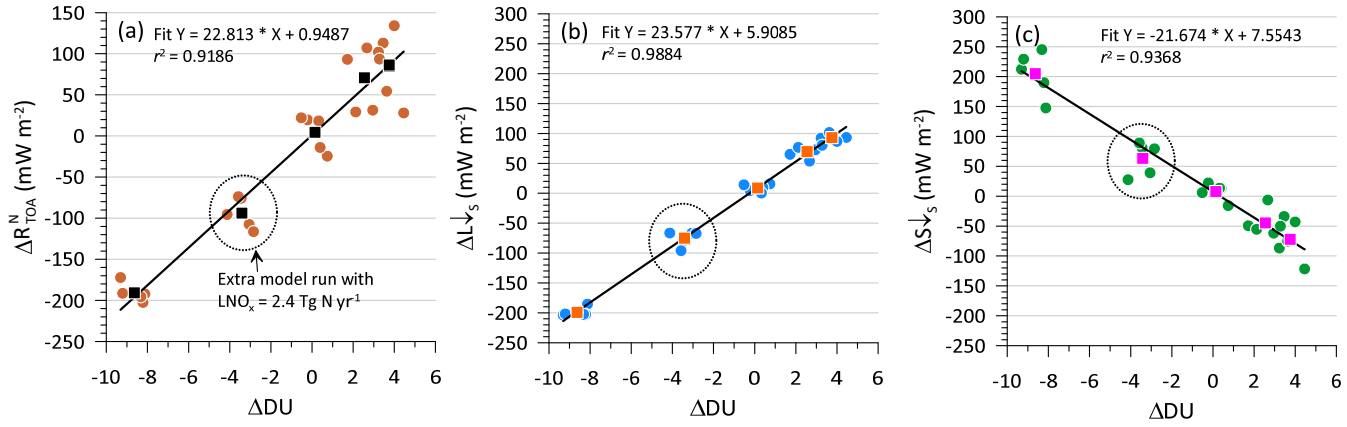

Figure 9: Change in the modelled (a) net downward total TOA radiation (ΔR^N_{TOA}), (b) incoming surface longwave radiation ($\Delta L{\downarrow}_S$) and (c) incoming surface shortwave radiation ($\Delta S{\downarrow}_S$), as a function of change in the modelled ~~tropospheric~~ O_3 column (ΔDU) relative to the Base model run. All runs except Run E (i.e., without the CH_4 radiation feedback) are considered. Results from an additional model simulation the same as Run C but with averaged LNO_x = 2.4 Tg N yr^{-1} are also plotted (enclosed in a dotted circle) to check linearity. The solid circles are the annual means whereas the squares are the mean over 2006–2010. The best fit line is based on all points.

The above changes in radiation were also examined as a function of changes in tropospheric O_3 burden (plots not shown). The slopes of these plots indicate that there is an increase of 3.3 mW m^{-2} (Tg O_3)$^{-1}$ in the net downward TOA radiation, an increase of 3.3 mW m^{-2} (Tg O_3)$^{-1}$ in the incoming surface longwave radiation, and a decrease of 3.1 mW m^{-2} (Tg O_3)$^{-1}$ in the incoming surface shortwave radiation.

In this paper, we have not explored atmospheric temperature response or any changes in atmospheric heating rates caused by the changes in the radiation balance due to the use of the improved parameterisations.

3.7~~5~~ LNO_x and the tropospheric lifetime of CH_4

~~LNO_x also affects the lifetime of CH_4 due to loss by OH () in the troposphere (Labrador et al., 2004). from Runs A, B, C, D, E and F are 7.61, 7.55, 6.97, 7.17, 6.97 and 9.26 years, respectively. Compared with the previous parameterisations, there is a relatively small decrease of 0.06 years in when the new oceanic O_3 dry deposition scheme is used and this decrease is 0.64 years when the improved LNO_x parameterisation is also used.~~

In Figure 10, the change in τ_{CH_4} plotted as a function of change in LNO_x suggests that there is a shortening of the global mean CH_4 lifetime by 0.31 years per Tg N yr^{-1} produced due to lightning. This change in τ_{CH_4} is equivalent to a change of –4.4% τ_{CH_4} per Tg N yr^{-1} produced due to lightning (with respect to the Run C value of τ_{CH_4}), which is close to the average –4.8 (range –6.8 to –2.4) % τ_{CH_4} per Tg N yr^{-1} given by Thornhill et al. (2021a) based on four other models. The uncertainty~~change~~ in τ_{CH_4} corresponding to an LNO_x uncertainty range of 5 ± 3~~2–8~~ Tg N yr^{-1} (Schumann and Huntrieser, 2007) would thus be ± 0.92~~1.9~~ years or ±13.5~~27~~% of τ_{CH_4} from Run C.

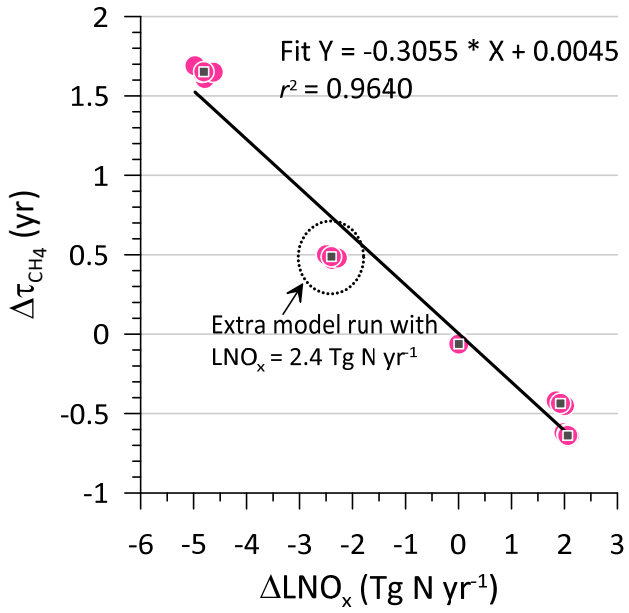

Figure 10: Same as Figure 8, except for change in the modelled CH_4 lifetime ($\Delta\tau_{CH_4}$).

3.8~~5~~ LNO_x and column integrated CN concentration

The change in in the modelled global column integrated CN concentration is plotted as a function of change in LNO_x in Figure 11. The slope of the linear fit suggests that there is an increase in the column CN concentration by 0.163 × 10^9 cm^{-2} per Tg N yr^{-1} LNO_x. Thus, the uncertainty in the column CN concentration corresponding to an LNO_x uncertainty range of 5 ± 3 Tg N yr^{-1} would be ± 0.49 × 10^9 cm^{-2} or ± 6.2% of the column CN concentration obtained from Run C.

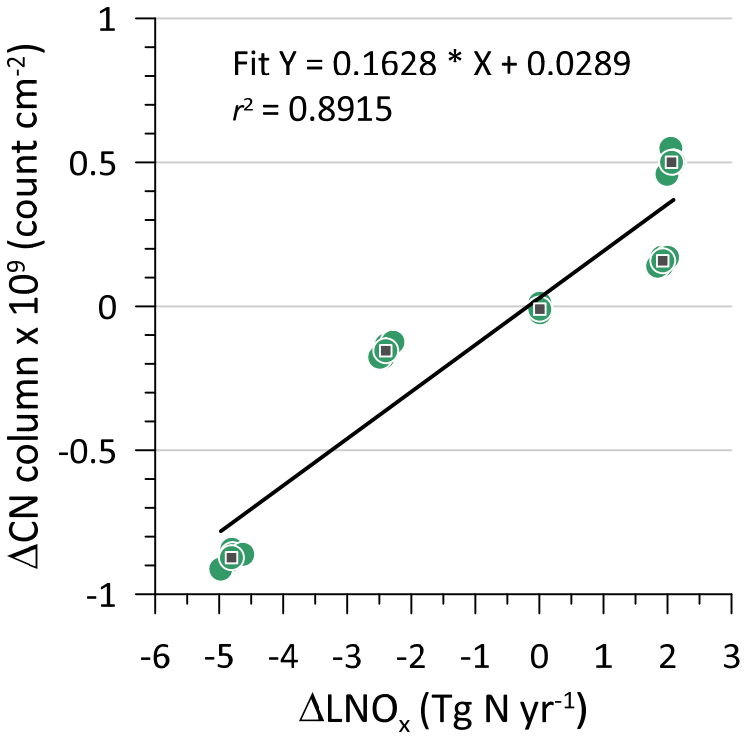

Figure 11: Same as Figure 8, except for change in the modelled global column integrated CN concentration.

3.9 LNO_x and radiative forcing in a broader context

The magnitude of the modelled net downward TOA radiation differences (ΔR^{N}_{TOA}) obtained (in section 3.3) can be put in the context of the IPCC AR6 reported anthropogenic ERF due to O_3 over the years 1750–2019 of 470 ± 230 mW m^{-2} (Forster et al., 2021), noting that the radiation differences calculated here are akin to instantaneous radiative forcing, which excludes any adjustments (e.g., adjustments causing circulation changes) unlike the ERF which is the sum of the IRF and the contribution from the adjustments. For example, the extra TOA radiation of 86.3 mW m^{-2} retained by the atmosphere when the new deposition and lightning flash-rate schemes are used, which represents the uncertainty in radiation due to two natural process representation in chemistry-climate models, is equivalent to 18% of the IPCC AR6 reported anthropogenic O_3 ERF of 470 mW m^{-2}.

Using the amount of radiative flux change per Tg N change in LNO_x from section 3.5 and assuming an uncertainty range of 5 ± 3 Tg N yr^{-1} in the global estimates of LNO_x suggested by Schumann and Huntrieser (2007), the corresponding uncertainty range in the net downward TOA radiation retained in the atmosphere could thus be as much as ± 119 mW m^{-2}. (Although these cannot be compared directly, this is equivalent to 50% of the IPCC AR6 reported anthropogenic O_3 ERF.) Similarly, the corresponding uncertainty range is ± 121 mW m^{-2} for the surface longwave radiation and ± 109 mW m^{-2} for the surface

shortwave radiation. Thus, the implications of this uncertainty in LNO_x for global climate modelling needs investigation and clarification.

As demonstrated in this study, the net instantaneous radiative forcing of LNO_x is positive with the enhanced O_3 production dominating over the reduced CH_4 lifetime. The emission-based ERF due to increases in anthropogenic NO_x emissions (from 1750 to 2019) based on chemistry-climate models is reported to be negative (at -0.29 ± 0.29 W m^{-2}), which is a net effect of a positive ERF through enhanced tropospheric O_3 production, a negative ERF through reduced CH_4 lifetime, and a small negative ERF contribution through formation of nitrate aerosols (Naik et al., 2021). ~~As demonstrated in this study, the net instantaneous radiative forcing of LNO_x is positive as the enhanced O_3 production dominates over the reduced CH_4 lifetime.~~ Notwithstanding the differences between ERF and IRF, this contrast between the LNO_x and anthropogenic NO_x forcings could at least be partially because (a) in the upper to middle troposphere within which LNO_x is generated, the production efficiency of O_3 per unit of NO_x is much larger than that close to the Earth's surface, where anthropogenic emissions are mostly released (Dahlmann et al., 2011) and (b) the historical anthropogenic NO_x emissions were accompanied by emissions of reactive VOCs which affects the subsequent chemistry.

As shown in section 3.7, LNO_x has a significant influence on the atmospheric lifetime of CH_4, and the value of LNO_x used within a model will influence the time integrated measures of radiative forcing including the ERF and the global warming potential (GWP) of anthropogenic CH_4. ~~The accepted atmospheric lifetime of CH_4 due to reaction with OH, soil removal and stratospheric oxidation is 7.8 years (average over 2000–2009) with a range of 6.5–8.8 years (Saunois et al., 2020). If the intermediate relationships are linear, then the uncertainty in LNO_x within the models would translate to an uncertainty of ±16% in the integrated measures of radiative forcing including the ERF and the GWP of anthropogenic CH_4.~~

Recent chemistry-climate modelling studies have explored changes in LNO_x in a future warming climate but there remains a large uncertainty depending on how lightning flash-rate parameterisations are formulated. All CMIP6 Earth system models use flash-rate parameterizations that use convective cloud-top height (as is the case in the present paper) and they project an increase in lightning and hence in LNO_x in a warmer world of 0.27–0.61 Tg N yr^{-1} per °C (Naik et al., 2021; Thornhill et al., 2021a). Flux-based flash-rate parameterisations, e.g., that by Finney et al. (2018) using upward cloud ice flux, predict decrease in lightning under climate change. Thus, despite the improvements in understanding, LNO_x remains a significant uncertainty for climate and earth system modelling.

4 Conclusions

The impact of recent ~~ly improved global~~ process-based improvements to oceanic O_3 dry deposition parameterisation~~s of oceanic O_3 dry deposition~~ (Luhar et al., 2018) and empirical improvements to lightning-generated NO_x parameterisation (Luhar et al., 2021) on radiative transfer was investigated via the use of the ACCESS-UKCA chemistry-climate model, which

includes radiative feedbacks of O_3 ~~, and~~ CH_4 ~~.~~ and aerosol. The main radiation components examined were the net downward ~~top of the atmosphere (~~TOA~~)~~ radiative flux, and the incoming longwave and shortwave radiation at the Earth's surface.

The effects of the LNO_x parameterisation change (which enhanced the LNO_x production from 4.8 to 6.9 Tg N yr^{-1}) were a factor of roughly 10 to 20 larger than those due to the dry deposition change. The two combined parameterisation changes increased the global tropospheric O_3 burden by 31.9 Tg O_3 (11.7%), increased the global O_3 column by 3.75 DU (13% of the tropospheric column or 1.2% of the total column), decreased the global mean tropospheric lifetime of CH_4 by 0.64 years (8.4%), increased the global column integrated aerosol number concentration by 0.5×10^9 cm^{-2} (6.7%), and impacted the cloud cover somewhat (zonal mean value by as much as ± 0.05%).

The use of the improved~~new~~ oceanic dry deposition scheme resulted in a relatively small increase of 4.3 mW m^{-2} in the all-sky net downward TOA radiative flux (i.e. or that much of radiation is retained by the atmosphere), but this increase was much larger at 86.3 mW m^{-2}, most of which longwave, when the improved LNO_x parameterisation was also used (this increase was 107.0 mW m^{-2} when the CH_4 radiative feedback is neglected). ~~(the latter increased the global LNO_x production to 6.9 from 4.8 Tg N yr^{-1}). This radiative flux difference is a net effect (107.0 – 20.7 mW m^{-2}) of an increase in O_3 and a decrease in CH_4 lifetime (by 0.64 years) against loss due to an increase in OH.~~ This change in the radiative flux ~~It~~ represents a measure of uncertainty in radiation due to two natural processes represented~~ation~~ in chemistry-climate models, and, for comparison, is equivalent to ~~–~~18% of the IPCC AR6 reported present-day anthropogenic radiative forcing due to O_3~~,~~ of 470 mW m^{-2}.

Similarly, with the two parameterisation changes, there was an increase of 93 mW m^{-2} in the all-sky downward longwave radiation and a decrease of 72 mW m^{-2} in the all-sky downward shortwave radiation at the Earth's surface. The changes in the all-sky downward shortwave radiation at the surface were consistent with the changes in the column aerosol number concentration and high-level cloud cover in response to the parameterisation changes.

The radiation changes due to the two improved parameterisations were larger in magnitude in the tropics than elsewhere. It was also found that when the default PR92 lightning flash-rate scheme (which underestimates the flash-rate distribution considerably over the ocean) was used with a uniform global scaling so as to give the total global LNO_x the same as the improved scheme, the improved scheme yielded a larger net downward TOA radiation by ~15 mW m^{-2}, which implies that how LNO_x is distributed spatially makes a difference to how the radiative transfer is impacted.

Based on the slopes of linear fits, ~~The changes in radiation components and CH_4 lifetime per unit change in LNO_x and column O_3 were also estimated based on the slopes of linear fits.~~with a per Tg N yr^{-1} increase in LNO_x, there was an increase of 39.6 mW m^{-2} in the net downward TOA radiation, an increase of 40.2 mW m^{-2} in the incoming surface longwave radiation, a decrease of 36.4 mW m^{-2} in the incoming surface shortwave radiation, and a shortening of CH_4 lifetime by 0.31 years (or ~ -4%).

The uncertainty range in the all-sky net downward TOA radiative flux due to ~~the uncertainty~~reported uncertainty range of 5 ± 3 Tg N yr^{-1} ~~-~~in global estimates of LNO_x could be as much as ± 119~~238~~ mW m^{-2}. This value is equivalent to 50% of the present-day anthropogenic radiative forcing due to O_3 ~~of 470 mW m^{-2}~~ reported by the IPCC AR6. The corresponding modelled uncertainty range is ± 121~~241~~ mW m^{-2} for the surface longwave radiation, ~~and~~ ± 109~~218~~ mW m^{-2} for the surface shortwave radiation, and ± 0.92 years for CH_4 lifetime.

~~The radiation changes due to the two improved parameterisations were larger in magnitude in the tropics than elsewhere. It was also found that when the default PR92 lightning flash rate scheme was used with a uniform scaling so as to give the total global LNO_x the same as the new scheme, the new scheme yielded a larger net downward TOA radiation by ~15 mW m^{-2}, which implies that how LNO_x is distributed spatially makes a difference to how the radiative transfer is impacted.~~

The above results highlight t~~T~~he impact of LNO_x on ~~the~~ tropospheric O_3 production, ~~and~~ methane lifetime and aerosol~~oxidising capacity is considerable~~, with ramifications for the~~on~~ Earth's radiation budget, and suggest that ~~. Similarly, LNO_x has a significant influence on the atmospheric lifetime of CH_4, and the value of LNO_x used within a model may influence the modelled ERF of anthropogenic CH_4.~~ the value of LNO_x used within a model will influence the modelled ERF and GWP of anthropogenic methane. The inter-model uncertainty in the ERF for methane will be contributed to by the model choices of LNO_x.

Data availability

The global model output (in NetCDF) from the ACCESS-UKCA simulations made can be obtained by contacting the corresponding author (Ashok Luhar: ashok.luhar@csiro.au). Radiation observations used for model comparison purposes were available from NASA's Clouds and the Earth's Radiant Energy System (CERES) EBAF (Energy Balanced and Filled) Ed4.1 dataset (https://ceres.larc.nasa.gov/data/).

Author contributions

All authors had the initial idea to carry out this work. AKL designed the study, performed the model simulations, analysed the model output and data, and prepared the manuscript. IEG co-designed the study, advised on various components of the paper, and contributed to paper writing. MTW advised on the model setup. All authors contributed to revisions of the paper.

Competing interests

The authors declare that they have no conflict of interest.

Acknowledgements

This work was partly supported by the Climate Systems Hub of the National Environmental Science Program (NESP) funded by the Australian Government, and was undertaken with the assistance of resources and services from the National Computational Infrastructure (NCI), which is supported by the Australian government. ERA-Interim data from the European Centre for Medium-Range Weather Forecasts (ECMWF) and radiation data from NASA's Clouds and the Earth's Radiant Energy System (CERES) were used in this research. We acknowledge Martin Dix of CSIRO for his help with model configuration issues, and Luke Abraham of the University of Cambridge and Mohit Dalvi of the U.K. Met Office for answering technical questions on the UM-UKCA model setup. We thank the two anonymous reviewers for their constructive comments.

References

Abraham, N. L., Archibald, A. T., Bellouin, N., Boucher, O., Braesicke, P., Bushell, A., Carslaw, K. S., Collins, W., Dalvi, M., Emmerson, K. M., Folberth, G., Haywood, J., Johnson, C., Kipling, Z., Macintyre, H., Mann, G. W., Telford, P. J., Merikanto, J., Morgenstern, O., O'Connor, F., Ordonez, C., Osprey, S., Pringle, K. J., Pyle, J. A., Rae, J. G. L., Reddington, C. L., Savage, D., Spracklen, D., Stier, P., and West, R.: Unified Model Documentation Paper No. 84 (http://www.ukca.ac.uk/images/b/b1/Umdp_084-umdp84.pdf): United Kingdom Chemistry and Aerosol (UKCA) Technical Description MetUM Version 8.4. UK Met Office, Exeter (UK), pp. 74, 2012.

Archibald, A. T., O'Connor, F. M., Abraham, N. L., Archer-Nicholls, S., Chipperfield, M. P., Dalvi, et al.: Description and evaluation of the UKCA stratosphere–troposphere chemistry scheme (StratTrop vn 1.0) implemented in UKESM1, Geosci. Model Dev., 13, 1223–1266, https://doi.org/10.5194/gmd-13-1223-2020, 2020.

Barten, J. G. M., Ganzeveld, L. N., Steeneveld, G.-J., and Krol, M. C.: Role of oceanic ozone deposition in explaining temporal variability in surface ozone at High Arctic sites, Atmos. Chem. Phys., 21, 10229–10248, https://doi.org/10.5194/acp-21-10229-2021, 2021.

Bellouin, N., Mann, G. W., Woodhouse, M. T., Johnson, C., Carslaw, K. S., and Dalvi, M.: Impact of the modal aerosol scheme GLOMAP-mode on aerosol forcing in the Hadley Centre Global Environmental Model, Atmos. Chem. Phys., 13, 3027–3044, https://doi.org/10.5194/acp-13-3027-2013, 2013.

Bi, D. H., Dix, M., Marsland, S. J., O'Farrell, S., Rashid, H. A., Uotila, P., Hirst, A. C., Kowalczyk, E., Golebiewski, M., Sullivan, A., Yan, H. L., Hannah, N., Franklin, C., Sun, Z. A., Vohralik, P., Watterson, I., Zhou, X. B., Fiedler, R., Collier, M., Ma, Y. M., Noonan, J., Stevens, L., Uhe, P., Zhu, H. Y., Griffies, S. M., Hill, R., Harris, C., and Puri, K.: The ACCESS coupled model: description, control climate and evaluation, Australian Meteorological and Oceanographic Journal, 63, 41–64, https://doi.org/10.22499/2.6301.004, 2013.

Boccippio, D. J.: Lightning scaling relations revisited, J. Atmos. Sci., 59, 1086–1104, https://doi.org/10.1175/1520-0469(2002)059<1086:LSRR>2.0.CO;2, 2002.

Chen, L., Yan, G., Wang, T., Ren, H., Calbó, J., Zhao, J., and McKenzie, R.: Estimation of surface shortwave radiation components under all sky conditions: Modeling and sensitivity analysis, Remote Sens. Environ., 123, 457–469, https://doi.org/10.1016/j.rse.2012.04.006, 2012.

Clifton, O. E., Fiore, A. M., Massman, W. J., Baublitz, C. B., Coyle, M., Emberson, L., et al.: Dry deposition of ozone over land: processes, measurement, and modelling, Reviews of Geophysics, 58, e2019RG000670, https://doi.org/10.1029/2019RG000670, 2020.

Dahlmann, K., Grewe, V., Ponater, M., and Matthes, S.: Quantifying the contributions of individual NO_x sources to the trend in ozone radiative forcing, Atmos. Environ., 45, 2860–2868, https://doi.org/10.1016/j.atmosenv.2011.02.071, 2011.

Dee, D. P., Uppala, S. M., Simmons, A. J., Berrisford, P., Poli, P., Kobayashi, S., Andrae, U., Balmaseda, M. A., Balsamo, G., Bauer, P., Bechtold, P., Beljaars, A. C. M., van de Berg, L., Bidlot, J., Bormann, N., Delsol, C., Dragani, R., Fuentes, M., Geer, A. J., Haimberger, L., Healy, S. B., Hersbach, H., Holm, E. V., Isaksen, L., Kallberg, P., Kohler, M., Matricardi, M., McNally, A. P., Monge-Sanz, B. M., Morcrette, J.-J., Park, B.-K., Peubey, C., de Rosnay, P., Tavolato, C., Thepaut, J.-N., and Vitarta, F.: The ERA-Interim reanalysis: configuration and performance of the data assimilation system, Q. J. Roy. Meteor. Soc., 137, 553–597, https://doi.org/10.1002/qj.828, 2011.

Desservettaz, M. J., Fisher, J. A., Luhar, A. K., Woodhouse, M. T., Bukosa, B., Buchholz, R. R., et al.: Australian fire emissions of carbon monoxide estimated by global biomass burning inventories: Variability and observational constraints, Journal of Geophysical Research: Atmospheres, 127, e2021JD035925, https://doi.org/10.1029/2021JD035925, 2022.

Edwards, J. M.: Efficient calculation of infrared fluxes and cooling rates using the two-stream equations, J. Atmos. Sci., 53, 1921–1932, https://doi.org/10.1175/1520-0469(1996)053<1921:ECOIFA>2.0.CO;2, 1996.

Edwards, J. M. and Slingo, A.: Studies with a flexible new radiation code. I: Choosing a configuration for a large-scale model, Q. J. Roy. Meteorol. Soc., 122, 689–719, https://doi.org/10.1002/qj.49712253107, 1996.

Fiddes, S. L., Woodhouse, M. T., Nicholls, Z., Lane, T. P., and Schofield, R.: Cloud, precipitation and radiation responses to large perturbations in global dimethyl sulfide, Atmos. Chem. Phys., 18, 10177–10198, https://doi.org/10.5194/acp-18-10177-2018, 2018.

Finney, D. L., Doherty, R. M., Wild, O., Stevenson, D. S., MacKenzie, I. A., and Blyth, A. M.: A projected decrease in lightning under climate change, Nat. Clim. Change, 8, 210–213, https://doi.org/10.1038/s41558-018-0072-6, 2018.

Forster, P., Storelvmo, T., Armour, K., Collins, W., Dufresne, J. L., Frame, D., Lunt, D. J., Mauritsen, T., Palmer, M. D., Watanabe, M., Wild, M., Zhang, H.: The Earth's Energy Budget, Climate Feedbacks, and Climate Sensitivity. In: Climate Change 2021: The Physical Science Basis. Contribution of Working Group I to the Sixth Assessment Report of the Intergovernmental Panel on Climate Change [Masson-Delmotte, V., Zhai, P., Pirani, A., Connors, S. L., Péan, C., Berger, S., Caud, N., Chen, Y., Goldfarb, L., Gomis, M. I., Huang, M., Leitzell, K., Lonnoy, E., Matthews, J. B. R., Maycock, T. K., Waterfield, T., Yelekçi, O., Yu, R., and Zhou, B. (eds.)]. Cambridge University Press. In Press, 2021.

Galbally, I. E. and Roy, C. R.: Destruction of ozone at the Earth's surface, Q. J. Roy. Meteor. Soc., 106, 599–620, https://doi.org/10.1002/qj.49710644915 1980.

Gauss, M., Myhre, G., Pitari, G., Prather, M. J., Isaksen, I. S. A., Berntsen, T. K., Brasseur, G. P., Dentener, F. J., Derwent, R. G., Hauglustaine, D. A., Horowitz, L. W., Jacob, D. J., Johnson, M., Law, K. S., Mickley, L. J., Muller, J.-F., Plantevin, P.-H., Pyle, J. A., Rogers, H. L., Stevenson, D. S., Sundet, J. K., van Weele, M., and Wild, O.: Radiative forcing in the 21st century due to ozone changes in the troposphere and the lower stratosphere, J. Geophys. Res., 108, 4292, https://doi.org/10.1029/2002JD002624, 2003.

Griffiths, P. T., Murray, L. T., Zeng, G., Shin, Y. M., Abraham, N. L., Archibald, A. T., Deushi, M., Emmons, L. K., Galbally, I. E., Hassler, B., Horowitz, L. W., Keeble, J., Liu, J., Moeini, O., Naik, V., O'Connor, F. M., Oshima, N., Tarasick, D., Tilmes, S., Turnock, S. T., Wild, O., Young, P. J., and Zanis, P.: Tropospheric ozone in CMIP6 simulations, Atmos. Chem. Phys., 21, 4187–4218, https://doi.org/10.5194/acp-21-4187-2021, 2021.

Jones, A. C., Hill, A., Remy, S., Abraham, N. L., Dalvi, M., Hardacre, C., Hewitt, A. J., Johnson, B., Mulcahy, J. P., and Turnock, S. T.: Exploring the sensitivity of atmospheric nitrate concentrations to nitric acid uptake rate using the Met Office's Unified Model, Atmos. Chem. Phys., 21, 15901–15927, https://doi.org/10.5194/acp-21-15901-2021, 2021.

Kato, S., Rose, F. G., Rutan, D. A., Thorsen, T. E., Loeb, N. G., Doelling, D. R., Huang, X., Smith, W. L., Su, W., and Ham, S.-H.: Surface irradiances of Edition 4.0 Clouds and the Earth's Radiant Energy System (CERES) Energy Balanced and Filled (EBAF) data product, Journal of Climate, 31, 4501-4527, https://doi.org/10.1175/JCLI-D-17-0523.1, 2018.

Labrador, L. J., von Kuhlmann, R., and Lawrence, M. G.: Strong sensitivity of the global mean OH concentration and the tropospheric oxidizing efficiency to the source of NO_x from lightning, Geophysical Research Letters, 31, L06102, https://doi.org/10.1029/2003GL019229, 2004.

Lamarque, J.-F., Bond, T. C., Eyring, V., Granier, C., Heil, A., Klimont, Z., Lee, D., Liousse, C., Mieville, A., Owen, B., Schultz, M. G., Shindell, D., Smith, S. J., Stehfest, E., Van Aardenne, J., Cooper, O. R., Kainuma, M., Mahowald, N., McConnell, J. R., Naik, V., Riahi, K., and van Vuuren, D. P.: Historical (1850–2000) gridded anthropogenic and biomass burning emissions of reactive gases and aerosols: methodology and application, Atmos. Chem. Phys., 10, 7017–7039, https://doi.org/10.5194/acp-10-7017-2010, 2010.

Lamarque, J.-F., Emmons, L. K., Hess, P. G., Kinnison, D. E., Tilmes, S., Vitt, F., Heald, C. L., Holland, E. A., Lauritzen, P. H., Neu, J., Orlando, J. J., Rasch, P. J., and Tyndall, G. K.: CAM-chem: description and evaluation of interactive atmospheric chemistry in the Community Earth System Model, Geosci. Model Dev., 5, 369–411, https://doi.org/10.5194/gmd-5-369-2012, 2012.

Lamarque, J.-F., Shindell, D. T., Josse, B., Young, P. J., Cionni, I., Eyring, V., Bergmann, D., Cameron-Smith, P., Collins, W. J., Doherty, R., Dalsoren, S., Faluvegi, G., Folberth, G., Ghan, S. J., Horowitz, L. W., Lee, Y. H., MacKenzie, I. A., Nagashima, T., Naik, V., Plummer, D., Righi, M., Rumbold, S. T., Schulz, M., Skeie, R. B., Stevenson, D. S., Strode, S., Sudo, K., Szopa, S., Voulgarakis, A., and Zeng, G.: The Atmospheric Chemistry and Climate Model Intercomparison Project (ACCMIP): overview and description of models, simulations and climate diagnostics, Geosci. Model Dev., 6, 179–206, https://doi.org/10.5194/gmd-6-179-2013, 2013.

Loades, D. C., Yang, M., Bell, T. G., Vaughan, A. R., Pound, R. J., Metzger, S., Lee, J. D., and Carpenter, L. J.: Ozone deposition to a coastal sea: comparison of eddy covariance observations with reactive air–sea exchange models, Atmos. Meas. Tech., 13, 6915–6931, https://doi.org/10.5194/amt-13-6915-2020, 2020.

Loeb, N. G., Doelling, D. R., Wang, H., Su, W., Nguyen, C., Corbett, J. G., Liang, L., Mitrescu, C., Rose, F. G., and Kato, S.: Clouds and the Earth's radiant energy system (CERES) energy balanced and filled (EBAF) top-of-atmosphere (TOA) edition-4.0 data product, Journal of Climate, 31, 895-918. https://doi.org/10.1175/JCLI-D-17-0208.1, 2018.

Luhar, A. K., Galbally, I. E., Woodhouse, M. T., and Thatcher, M.: An improved parameterisation of ozone dry deposition to the ocean and its impact in a global climate-chemistry model, Atmos. Chem. Phys., 17, 3749–3767, https://doi.org/10.5194/acp-17-3749-2017, 2017.

Luhar, A. K., Woodhouse, M. T., and Galbally, I. E.: A revised global ozone dry deposition estimate based on a new two-layer parameterisation for air–sea exchange and the multi-year MACC composition reanalysis, Atmos. Chem. Phys., 18, 4329–4348, https://doi.org/10.5194/acp-18-4329-2018, 2018.

Luhar, A. K., Galbally, I. E., Woodhouse, M. T., and Abraham, N. L.: Assessing and improving cloud-height-based parameterisations of global lightning flash rate, and their impact on lightning-produced NO_x and tropospheric composition in a chemistry–climate model, Atmos. Chem. Phys., 21, 7053–7082, https://doi.org/10.5194/acp-21-7053-2021, 2021.

Mann, G. W., Carslaw, K. S., Spracklen, D. V., Ridley, D. A., Manktelow, P. T., Chipperfield, M. P., Pickering, S. J., and Johnson, C. E.: Description and evaluation of GLOMAP-mode: a modal global aerosol microphysics model for the UKCA composition-climate model, Geosci. Model Dev., 3, 519–551, https://doi.org/10.5194/gmd-3-519-2010, 2010.

Mao, J., Paulot, F., Jacob, D. J., Cohen, R. C., Crounse, J. D., Wennberg, P. O., Keller, C. A., Hudman, R. C., Barkley, M. P., and Horowitz, L. W.: Ozone and organic nitrates over the eastern United States: Sensitivity to isoprene chemistry, J. Geophys. Res.-Atmos., 118, 11256–11268, https://doi.org/10.1002/jgrd.50817, 2013.

Martin, R. V., Sauvage, B., Folkins, I., Sioris, C. E., Boone, C., Bernath, P., and Ziemke, J.: Space-based constraints on the production of nitric oxide by lightning, J. Geophys. Res., 112, D09309, https://doi.org/10.1029/2006JD007831, 2007.

Murray, L. T.: Lightning NO_x and impacts on air quality, Current Pollution Reports, 2, 115–133, https://doi.org/10.1007/s40726-016-0031-7, 2016.

Neu, J. L., Prather, M. J., and Penner, J. E.: Global atmospheric chemistry: Integrating over fractional cloud cover, J. Geophys. Res., 112, D11306, https://doi.org/10.1029/2006JD008007, 2007.

Naik, V., Voulgarakis, A., Fiore, A. M., Horowitz, L. W., Lamarque, J.-F., Lin, M., Prather, M. J., Young, P. J., Bergmann, D., Cameron-Smith, P. J., Cionni, I., Collins, W. J., Dalsøren, S. B., Doherty, R., Eyring, V., Faluvegi, G., Folberth, G. A., Josse, B., Lee, Y. H., MacKenzie, I. A., Nagashima, T., van Noije, T. P. C., Plummer, D. A., Righi, M., Rumbold, S. T., Skeie, R., Shindell, D. T., Stevenson, D. S., Strode, S., Sudo, K., Szopa, S., and Zeng, G.: Preindustrial to present-day changes in tropospheric hydroxyl radical and methane lifetime from the Atmospheric Chemistry and Climate Model Intercomparison Project (ACCMIP), Atmos. Chem. Phys., 13, 5277–5298, https://doi:10.5194/acp-13-5277-2013, 2013.

Naik, V., Szopa, S., Adhikary, B., Artaxo, P., Berntsen, T., Collins, W. D., Fuzzi, S., Gallardo, L., Kiendler Scharr, A., Klimont, Z., Liao, H., Unger, N., Zanis, P.: Short-Lived Climate Forcers. In: Climate Change 2021: The Physical Science Basis. Contribution of Working Group I to the Sixth Assessment Report of the Intergovernmental Panel on Climate Change [Masson-Delmotte, V., Zhai, P., Pirani, A., Connors, S. L., Péan, C., Berger, S., Caud, N., Chen, Y., Goldfarb, L., Gomis, M. I., Huang, M., Leitzell, K., Lonnoy, E., Matthews, J. B. R., Maycock, T. K., Waterfield, T., Yelekçi, O., Yu, R., and Zhou, B. (eds.)]. Cambridge University Press. In Press, 2021.

Nault, B. A., Laughner, J. L.,Wooldridge, P. J., Crounse, J. D., Dibb, J., Diskin, G., Peischl, J., Podolske, J. R., Pollack, I. B., Ryerson, T. B., Scheuer, E., Wennberg, P. O., and Cohen, R. C.: Lightning NO_x emissions: reconciling measured and modeled estimates with updated NO_x Chemistry, Geophys. Res. Lett., 44, 9479–9488, https://doi.org/10.1002/2017GL074436, 2017.

Olivier, J., Peters, J., Granier, C., Petron, G., Muller, J. F., and Wallens, S.: Present and future surface emissions of atmospheric compounds, POET Report #2 EU project EVK2–1999–00011, 2003 (http://accent.aero.jussieu.fr/POET_metadata.php, last access: 25 May 2022).

Oreopoulos, L. and Khairoutdinov, M.: Overlap properties of clouds generated by a cloud-resolving model, J. Geophys. Res. 108, 4479, https://doi.org/10.1029/2002JD003329, 2003.

Pound, R. J., Sherwen, T., Helmig, D., Carpenter, L. J., and Evans, M. J.: Influences of oceanic ozone deposition on tropospheric photochemistry, Atmos. Chem. Phys., 20, 4227–4239, https://doi.org/10.5194/acp-20-4227-2020, 2020.

Price, C. and Rind, D.: A simple lightning parameterization for calculating global lightning distributions, J. Geophys. Res.-Atmos., 97, 9919–9933, https://doi.org/10.1029/92JD00719, 1992.

Rap, A., Richards, N. A. D., Forster, P. M., Monks, S. A., Arnold, S. R., and Chipperfield, M. P.: Satellite constraint on the tropospheric ozone radiative effect, Geophys. Res. Lett., 42, 5074–5081, https://doi.org/10.1002/2015GL064037, 2015.

~~Saunois, M., Stavert, A. R., Poulter, B., Bousquet, P., Canadell, J. G., Jackson, R. B., et al.: The global methane budget 2000–2017, Earth System Science Data, 12, 1561–1623, https://doi.org/10.5194/essd-12-1561-2020, 2020.~~

Schumann, U. and Huntrieser, H.: The global lightning-induced nitrogen oxides source, Atmos. Chem. Phys., 7, 3823–3907, https://doi.org/10.5194/acp-7-3823-2007, 2007.

Sindelarova, K., Granier, C., Bouarar, I., Guenther, A., Tilmes, S., Stavrakou, T., Müller, J.-F., Kuhn, U., Stefani, P., and Knorr, W.: Global data set of biogenic VOC emissions calculated by the MEGAN model over the last 30 years, Atmos. Chem. Phys., 14, 9317–9341, https://doi.org/10.5194/acp-14-9317-2014, 2014.

Stephens, G. L., Li, J., Wild, M., Clayson, C. A., Loeb, N. G., Kato, S., L'Ecuyer, T., Stackhouse, P. W., Lebsock, M., and Andrews, T.: An update on Earth's energy balance in light of the latest global observations, Nat. Geosci., 5, 691–696, https://doi.org/10.1038/ngeo1580, 2012.

Stevenson, D. S., Young, P. J., Naik, V., Lamarque, J.-F., Shindell, D. T., Voulgarakis, A., Skeie, R. B. et al.: Tropospheric ozone changes, radiative forcing and attribution to emissions in the Atmospheric Chemistry and Climate Model Intercomparison Project (ACCMIP), Atmos. Chem. Phys., 13, 3063–3085, https://doi.org/10.5194/acp-13-3063-2013, 2013.

Telford, P. J., Abraham, N. L., Archibald, A. T., Braesicke, P., Dalvi, M., Morgenstern, O., O'Connor, F. M., Richards, N. A. D., and Pyle, J. A.: Implementation of the Fast-JX Photolysis scheme (v6.4) into the UKCA component of the MetUM chemistry-climate model (v7.3), Geosci. Model Dev., 6, 161–177, https://doi.org/10.5194/gmd-6-161-2013, 2013.

Thornhill, G., Collins, W., Olivié, D., Skeie, R. B., Archibald, A., Bauer, S., Checa-Garcia, R., Fiedler, S., Folberth, G., Gjermundsen, A., Horowitz, L., Lamarque, J.-F., Michou, M., Mulcahy, J., Nabat, P., Naik, V., O'Connor, F. M., Paulot, F., Schulz, M., Scott, C. E., Séférian, R., Smith, C., Takemura, T., Tilmes, S., Tsigaridis, K., and Weber, J.: Climate-driven chemistry and aerosol feedbacks in CMIP6 Earth system models, Atmos. Chem. Phys., 21, 1105–1126, https://doi.org/10.5194/acp-21-1105-2021, 2021a.

Thornhill, G. D., Collins, W. J., Kramer, R. J., Olivié, D., Skeie, R. B., O'Connor, F. M., Abraham, N. L., Checa-Garcia, R., Bauer, S. E., Deushi, M., Emmons, L. K., Forster, P. M., Horowitz, L. W., Johnson, B., Keeble, J., Lamarque, J.-F., Michou, M., Mills, M. J., Mulcahy, J. P., Myhre, G., Nabat, P., Naik, V., Oshima, N., Schulz, M., Smith, C. J., Takemura, T., Tilmes, S., Wu, T., Zeng, G., and Zhang, J.: Effective radiative forcing from emissions of reactive gases and aerosols – a multi-model comparison, Atmos. Chem. Phys., 21, 853–874, https://doi.org/10.5194/acp-21-853-2021, 2021b.

Tost, H.: Chemistry–climate interactions of aerosol nitrate from lightning, Atmos. Chem. Phys., 17, 1125–1142, https://doi.org/10.5194/acp-17-1125-2017, 2017.

van der Werf, G. R., Randerson, J. T., Giglio, L., van Leeuwen, T. T., Chen, Y., Rogers, B. M., Mu, M., van Marle, M. J. E., Morton, D. C., Collatz, G. J., Yokelson, R. J., and Kasibhatla, P. S.: Global fire emissions estimates during 1997–2016, Earth Syst. Sci. Data, 9, 697–720, https://doi.org/10.5194/essd-9-697-2017, 2017.

van Vuuren, D. P., Edmonds, J., Kainuma, M., Riahi, K., Thomson, A., Hibbard, K., Hurtt, G. C., Kram, T., Krey, V., Lamarque, J. F., Masui, T., Meinshausen, M., Nakicenovic, N., Smith, S. J., and Rose, S. K.: The representative concentration pathways: An overview, Climatic Change, 109, 5–31, https://doi.org/10.1007/s10584-011-0148-z, 2011.

Walters, D. N., Williams, K. D., Boutle, I. A., Bushell, A. C., Edwards, J. M., Field, P. R., Lock, A. P., Morcrette, C. J., Stratton, R. A., Wilkinson, J. M., Willett, M. R., Bellouin, N., Bodas-Salcedo, A., et al.: The Met Office Unified Model Global Atmosphere 4.0 and JULES Global Land 4.0 configurations, Geosci. Model Dev., 7, 361–386, https://doi.org/10.5194/gmd-7-361-2014, 2014.

Wang, K., and Dickinson, R. E.: Global atmospheric downward longwave radiation at the surface from ground-based observations, satellite retrievals, and reanalyses, Reviews of Geophysics, 51, 150-185, https://doi.org/10.1002/rog.20009, 2013.

Wesely, M.: Parameterization of surface resistances to gaseous dry deposition in regional-scale numerical-models, Atmos. Environ., 23, 1293–1304, https://doi.org/10.1016/j.atmosenv.2007.10.058, 1989.

Woodhouse, M. T., Luhar, A. K., Stevens, L., Galbally, I., Thatcher, M., Uhe, P., Wolff, H., Noonan, J., and Molloy, S.: Australian reactive-gas emissions in a global chemistry-climate model and initial results, Air Quality and Climate Change, 49, 31-38, 2015.

Woodward, S.: Modeling the atmospheric life cycle and radiative impact of mineral dust in the Hadley Centre climate model, J. Geophys. Res.-Atmos., 106, 18155–18166, https://doi.org/10.1029/2000JD900795, 2001.

Young, P. J., Archibald, A. T., Bowman, K. W., Lamarque, J.-F., Naik, V., Stevenson, D. S., Tilmes, S., Voulgarakis, A., Wild, O., Bergmann, D., Cameron-Smith, P., Cionni, I., Collins, W. J., Dalsøren, S. B., Doherty, R. M., Eyring, V., Faluvegi, G., Horowitz, L. W., Josse, B., Lee, Y. H., MacKenzie, I. A., Nagashima, T., Plummer, D. A., Righi, M., Rumbold, S. T., Skeie, R. B., Shindell, D. T., Strode, S. A., Sudo, K., Szopa, S., and Zeng, G.: Pre-industrial to end 21st century projections of tropospheric ozone from the Atmospheric Chemistry and Climate Model Intercomparison Project (ACCMIP), Atmos. Chem. Phys., 13, 2063–2090, https://doi.org/10.5194/acp-13-2063-2013, 2013.

Zhong, W. and Haigh, J. D.: An efficient and accurate correlated-k parameterization of infrared radiative transfer for troposphere–stratosphere–mesosphere GCMs, Atmos. Sci. Lett., 1, 125–135, https://doi.org/10.1006/asle.2000.0022, 2000.

Zhong, W., Osprey, S. M., Gray, L. J., and Haigh, J. D.: Influence of the prescribed solar spectrum on calculations of atmospheric temperature, Geophys. Res. Lett., 35, L22813, https://doi.org/10.1029/2008GL035993, 2008.